Chapter 9

Entanglement of spin waves among four quantum memories

This chapter is largely based on ref. [33]. Reference [33] refers to the then current literature in 2010 at the time of publication.

9.1 Introduction

Diverse applications in quantum information science require coherent control of the generation, storage, and transfer of entanglement among spatially separated physical systems (refs. [1–6], see also chapter 1). Despite its inherently multipartite nature, entanglement has been studied primarily for bipartite systems [3], where remarkable progress has been made in harnessing physical processes to generate 'push-button' and 'heralded' entanglement (refs. [27–29,32,285,286], chapters 3–5), as well as to map entangled states to and from atoms, photons, and phonons (refs. [30,31], chapter 6).

For multipartite systems, the 'size' of a physical state, described by the system's density matrix $\hat{\rho}_N$, grows exponentially with the number of subsystems N and makes the entangled states exceedingly difficult to represent with classical information. Importantly, this complexity for $\hat{\rho}_N$ increases the potential utility of multipartite entanglement in quantum information science, including for quantum algorithms [2,3] and simulation [5]. Redundant encoding of quantum information into multipartite entangled states enables quantum error correction and fault-tolerant computation [2,3]. Intricate long-range correlation of many-body systems is intimately intertwined with the behavior of multipartite entanglement [39,40]. In addition, mobilizing multipartite entanglement across quantum networks could lead to novel quantum phase transitions for the network [6].

Counterposed to these opportunities, the complex structure of multipartite entanglement presents serious challenges both for its formal characterization and physical realization [3,40,110,208]. Indeed, there are relatively few examples of laboratory systems that have successfully generated multipartite entanglement [35,275–277,287,288]. Most works have considered the entanglement for spin systems, notably trapped ions [275,276], which are applicable to the matter nodes of quantum networks. But the methodologies for verifying multipartite entangle-

ment are problematic for the infinite-dimensional bosonic systems of the quantum channels (e.g., multipartite quadrature[287,288] and number-state[35] entanglement for optical modes (chapter 8)). *A posteriori* multipartite entanglement has been inferred from a small subset of preferred detection events of photons from parametric down-conversion[277].

In addition to the characterization of multipartite entanglement, an important capability for quantum networks is provided by quantum interfaces capable of generating, storing, and dynamically allocating the entanglement of matter nodes into photonic channels (see ref.[104] and references therein). In this chapter, as illustrated in Fig. 9.1a, we introduce such a quantum interface for quadripartite entangled states based upon coherent, collective emission from matter to light. We present a systematic study of the generation and storage of quadripartite entangled states of spin-waves in a set of four nodes of atomic memories, as well as of the coherent transfer of the entangled components of the material state into individual photonic channels. We observe transitions of M to $(M-1)$-partite entangled states via controlled spin-wave statistics of the atomic memories, as well as the dynamic evolution of multipartite entanglement in a dissipative environment, from fully quadripartite entangled to unentangled.

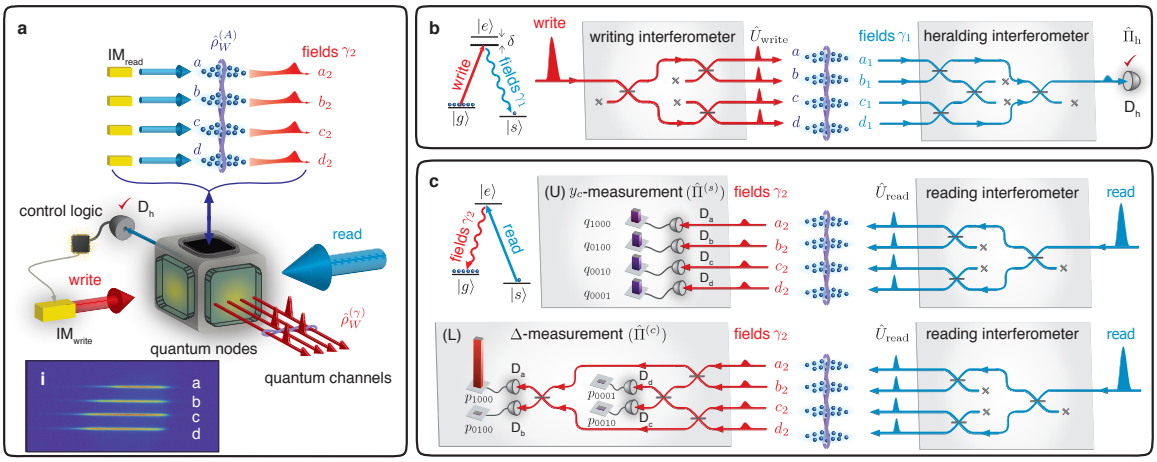

Figure 9.1: **Overview of the experiment. a,** Quantum interfaces for multipartite quantum networks. Inset **i**, a fluorescence image of the laser-cooled atomic ensembles $\{a, b, c, d\}$ that become entangled (section 9.9). **b,** Entanglement generation. A weak write laser is split into four components to excite the atomic ensembles via parametric interactions $\hat{U}_{\text{write}}$ (chapter 2), leading to Raman scattered fields $\gamma_1 = \{a_1, b_1, c_1, d_1\}$ emitted by the ensembles. Entangled state $\hat{\rho}_W^{(A)}$ for four atomic ensembles $\epsilon = \{a, b, c, d\}$ (Eq. 9.1) is heralded by a projective measurement $\hat{\Pi}_h$ at detector D_h, derived from quantum interference of four fields γ_1 in the heralding interferometer. **c,** Quantum-state exchange and entanglement verification. Read lasers are applied to the ensembles to coherently transform the atomic entangled state $\hat{\rho}_W^{(A)}$ into quadripartite entangled beams of light $\hat{\rho}_W^{(\gamma)}$ (Eq. 9.2) via quantum-state transfers, $\hat{U}_{\text{read}}$ (chapter 2), with each beam propagating through quantum channels $\gamma_2 = \{a_2, b_2, c_2, d_2\}$. (U) Upper panel for y_c-measurement—The quantum statistics $\{q_{ijkl}\}$ for the individual modes of $\hat{\rho}_W^{(\gamma)}$ with $i, j, k, l \in \{0, 1\}$ photons are measured with projectors $\{\hat{\Pi}_i^{(s)}\}$ at detectors $D_{a,b,c,d}$. (L) Lower panel for Δ-measurement—Mutual coherences for $\hat{\rho}_W^{(A)}$ are accessed with projectors $\{\hat{\Pi}_i^{(c)}\}$ from detection statistics $\{p_{ijkl}\}$ at $D_{a,b,c,d}$. Further details are given in section 9.12.

9.2 Quantum interface between light and matter for quadripartite entangled states

Our experiment proceeds in four steps (see section 9.10). First, in step (1) an entangled state $\hat{\rho}_W^{(A)}$ of four atomic ensembles is generated by quantum interference in a quantum measurement[4,27] (Fig. 9.1b). Given a photoelectric detection event at D_h, the conditional atomic state is ideally a quadripartite entangled state $\hat{\rho}_W^{(A)} = |W\rangle_A\langle W|$ with

$$|W\rangle_A = \tfrac{1}{2}[(|\overline{s}_a, \overline{g}_b, \overline{g}_c, \overline{g}_d\rangle + e^{i\phi_1}|\overline{g}_a, \overline{s}_b, \overline{g}_c, \overline{g}_d\rangle) + e^{i\phi_2}(|\overline{g}_a, \overline{g}_b, \overline{s}_c, \overline{g}_d\rangle + e^{i\phi_3}|\overline{g}_a, \overline{g}_b, \overline{g}_c, \overline{s}_d\rangle)], \tag{9.1}$$

whose single quantum spin-wave $|\overline{s}_\epsilon\rangle$ is coherently shared among four ensembles $\epsilon = \{a, b, c, d\}$. These entangled states are known as W-states, comprised of atomic ground states $|\overline{g}_\epsilon\rangle = |g\cdots g\rangle_\epsilon$ and single collective excitations $|\overline{s}_\epsilon\rangle = \frac{1}{\sqrt{N_{A,\epsilon}}}\sum_{i=1}^{N_{A,\epsilon}}|g\cdots s_i\cdots g\rangle_\epsilon$, where $N_{A,\epsilon}$ is the number of atoms in ensemble ϵ.

After the heralding event, step (2) consists of storage of $\hat{\rho}_W^{(A)}$ in the ensembles for a user-controlled time τ. At the end of this interval, step (3) is initiated with read beams to coherently transfer the entangled atomic components of $\hat{\rho}_W^{(A)}$ into a quadripartite entangled state of light $\hat{\rho}_W^{(\gamma)} = |W\rangle_\gamma\langle W|$ via cooperative emissions[4] (Fig. 9.1c), where

$$|W\rangle_\gamma = \frac{1}{2}[(|1000\rangle + e^{i\phi_1'}|0100\rangle) + e^{i\phi_2'}(|0010\rangle + e^{i\phi_3'}|0001\rangle)]. \tag{9.2}$$

This photonic state is a mode-entangled W-state (refs.[35,38], chapters 7–8), which shares a single delocalized photon among four spatially separated optical modes $\gamma_2 = \{a_2, b_2, c_2, d_2\}$.

9.3 Characterization of quadripartite entangled states via quantum uncertainty relations

Finally, in step (4) we characterize the heralded entanglement for $\hat{\rho}_W^{(\gamma)}$ from complementary measurements of photon statistics and coherence[35,38] (Fig. 9.1c) via the techniques developed in chapters 7–8. In particular, we consider a reduced density matrix $\hat{\rho}_r = p_0\hat{\rho}_0 + p_1\hat{\rho}_1 + p_{\geq 2}\hat{\rho}_{\geq 2}$ containing up to one photon per mode, which leads to a lower bound for the entanglement of the actual physical states $\{\hat{\rho}_W^{(A)}, \hat{\rho}_W^{(\gamma)}\}$. Here, $\{p_0, p_1, p_{\geq 2}\}$ are the probabilities for 0 and 1-photon $\hat{\rho}_{0,1}$, and higher-order subspaces $\hat{\rho}_{\geq 2}$, which can be populated for any realistic system. As illustrated in the upper panel of Fig. 9.1c, we characterize the statistical contamination for $\hat{\rho}_W^{(\gamma)}$ due to $\{\hat{\rho}_0, \hat{\rho}_{\geq 2}\}$ with a normalized measure[38], namely $y_c \equiv \frac{8}{3}\frac{p_{\geq 2}p_0}{p_1^2}$, ranging from $y_c = 0$ for a

single excitation to $y_c = 1$ for balanced coherent states, by detecting the photon statistics q_{ijkl} of γ_2 at the output faces of the ensembles.

We also quantify the mutual coherences for $\hat{\rho}_W^{(\gamma)}$ by measuring photon probabilities $\{p_{1000}, p_{0100}, p_{0010}, p_{0001}\}$ at the outputs of the verification (v) interferometer. We determine the sum uncertainty $\Delta \equiv \sum_{i=1}^{N=4} \langle(\hat{\Pi}_i^{(c)})^2 - \langle\hat{\Pi}_i^{(c)}\rangle^2\rangle$ for the variables $\{\hat{\Pi}_i^{(c)}\} = \{|W_i\rangle_v\langle W_i|\}$, which project $\hat{\rho}_r$ onto a set of four orthonormal W-states $\{|W_i\rangle_v\}$ with phases $\{\beta_1, \beta_2, \beta_3\}_v$ selected by the actively stabilized paths in the verification interferometer (section 9.12.2). Hence, for the ideal W-state (Eq. 9.2) with $\beta_i = \phi_i'$, we have $\Delta = 0$ associated with $p_{1000} = 1$ and $p_{0100} = p_{0010} = p_{0001} = 0$, as observed in the bar plots of the lower panel of Fig. 9.1c for $y_c = 0.04 \pm 0.01$. In contrast, mixed states with no phase coherences would result in balanced probabilities ($p_{1000} = p_{0100} = p_{0010} = p_{0001} = 1/4$) and $\Delta = 0.75$.

The pair $\{\Delta, y_c\}$ thereby defines the parameter space for the multipartite entanglement employed in our experiment, with the entanglement parameters $\{\Delta, y_c\}$ serving as a nonlocal, nonlinear entanglement witness (ref.[38], chapter 7). Our criterion for 'genuine' M-partite entanglement takes the most stringent form of nonseparability[208] and excludes all weaker forms of entanglement (section 9.13). Specifically, for a given value of y_c, we determine the boundary $\Delta_b^{(M-1)}$ for the minimal uncertainty possible for all states containing at most $(M-1)$-mode entanglement and their mixtures (section 9.13.3). For our quadripartite states $N = 4$, we derive $\{\Delta_b^{(3)}, \Delta_b^{(2)}, \Delta_b^{(1)}\}$ for tripartite, bipartite entangled, and fully separable states, as functions of y_c. Thus, a measurement of quantum statistics y_c and the associated coherence Δ with $\Delta < \Delta_b^{(1,2,3)}$ manifestly confirms the presence of genuine $M = 4$ partite entanglement (refs.[35,38], chapters 7–8). Furthermore, we can unambiguously distinguish genuine M and $(M-1)$-partite entangled states for any $M \leq N$ by observing Δ below $\Delta_b^{(M-1)}$.

9.4 Quadripartite entanglement among four atomic ensembles

Fig. 9.2 presents our results for quadripartite entanglement for storage time $\tau_0 = 0.2$ μs. We first investigate off-diagonal coherence for the purportedly entangled atomic and photonic states, $\{\hat{\rho}_W^{(A)}, \hat{\rho}_W^{(\gamma)}\}$, in Fig. 9.2a. As the bipartite phase β_2 is varied, we observe interferences in $\{p_{1000}, p_{0100}, p_{0010}, p_{0001}\}$, and hence a variation in Δ, that results from the coherence between the bipartite entangled components of $\hat{\rho}_W^{(\gamma)}$ for the modes $\{a_2, b_2\}$ and $\{c_2, d_2\}$. Furthermore, for optimal settings of β_2, the observed values of Δ (black points) fall below the bounds $\{\Delta_b^{(3)}, \Delta_b^{(2)}, \Delta_b^{(1)}\}$ (red, green, purple bands) for $y_c = 0.06 \pm 0.02$, and signal the generation of a fully quadripartite entangled state. The observed quadripartite entanglement arises from the intrinsic indistinguishability of probability amplitudes for one collective excitation $|\overline{s}_\epsilon\rangle$ among the four ensembles. We also present results from a control experiment with a 'crossed' state $\hat{\rho}_\times^{(A)}$ (orange points) that consists of an incoherent mixture of entangled pairs $\{a, b\}$ and $\{c, d\}$ (see section 9.5.1).

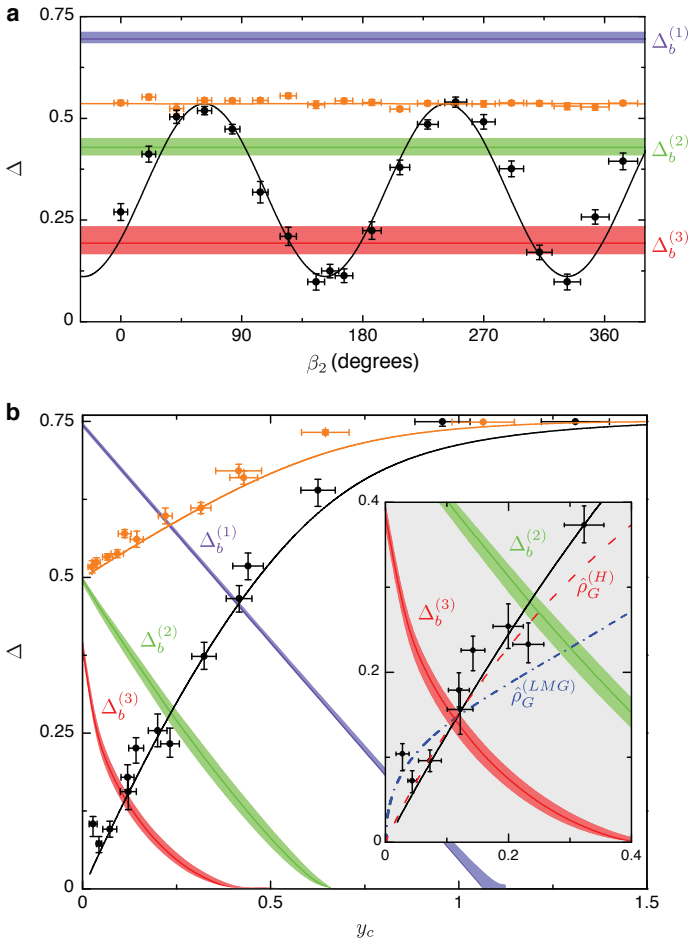

Figure 9.2: **Quadripartite entanglement among four atomic ensembles. a,** Quantum interference between the bipartite entangled pairs of the full quadripartite state (black points) as a function of bipartite phase β_2. **b,** Exploring the entanglement space $\{\Delta, y_c\}$ for quadripartite states. By controlling the spin-wave statistics, we observe transitions from quadripartite, to tripartite, to bipartite entangled states, and to fully separable states (black points). We also display our results for the 'crossed' quantum state $\hat{\rho}_{\times}^{(A)}$ (orange points), as further discussed in section 9.5.1. Inset, expanded view of entanglement parameters $\{\Delta, y_c\}$. Results for entanglement thermalization $\{\Delta^{(T)}, y_c^{(T)}\}$ of the spin systems $\hat{\rho}_G^{(\mathrm{H})}$ ($\hat{\rho}_G^{(\mathrm{LMG})}$) are shown by the red dashed (blue dash-dotted) line. The red, green, and purple bands represent the minimum uncertainties for 3-mode ($\Delta_b^{(3)}$) and 2-mode entanglement ($\Delta_b^{(2)}$), and for fully separable states ($\Delta_b^{(1)}$), with thicknesses of the bands from the central lines corresponding to ± 1 s.d. of the bounds $\{\Delta_b^{(3)}, \Delta_b^{(2)}, \Delta_b^{(1)}\}$ (section 9.13.3). In all cases, error bars for the data reflect the statistical and systematic uncertainties, as further detailed in section 9.13.4.

9.5 Statistical transitions for multipartite entangled spin waves

Next, we characterize $\hat{\rho}_W^{(\gamma)}$ (and $\hat{\rho}_W^{(A)}$) over the full parameter space $\{\Delta, y_c\}$. In a regime of weak excitation ($\xi \ll 1$) for the ensemble-field pairs $\{\epsilon, \gamma_1\}$, the heralded state $\hat{\rho}_W^{(A)}$ is approximately

$$\hat{\rho}_W^{(A)}(\tau = 0) \simeq (1 - 3\xi)|W\rangle_A\langle W| + 3\xi\hat{\rho}_{\geq 2}^{(A)} + \mathcal{O}(\xi^2), \tag{9.3}$$

where $\hat{\rho}_{\geq 2}^{(A)}$ includes uncorrelated spin-waves with two or more quanta in the set of four ensembles due to atomic noise. For $\xi \to 0$, a heralding event at D_h leads to a state with high fidelity to $|W\rangle_A$ stored in the four ensembles. However, for increasing ξ, $\hat{\rho}_{\geq 2}^{(A)}$ becomes important, leading to modifications of the spin-wave statistics for $\hat{\rho}_W^{(A)}$ and thereby to the entanglement parameters $\{\Delta^{\text{th}}, y_c^{\text{th}}\}$. Hence, by varying ξ via the overall intensity for the write beam, we adjust the quantum statistics y_c and coherence Δ of the entangled states $\{\hat{\rho}_W^{(A)}, \hat{\rho}_W^{(\gamma)}\}$.

This procedure is employed in Fig. 9.2b to parametrically increase $\{\Delta, y_c\}$ in tandem. As y_c is raised from $y_c \simeq 0$ in the quantum domain to the classical regime with $y_c \simeq 1$, we observe transitions of the directly measured photonic states $\hat{\rho}_W^{(\gamma)}$ (black points) from fully quadripartite entangled ($\Delta < \Delta_b^{(3)}$) to tripartite entangled ($\Delta_b^{(3)} < \Delta < \Delta_b^{(2)}$), to bipartite entangled ($\Delta_b^{(2)} < \Delta < \Delta_b^{(1)}$), and finally to fully separable states ($\Delta_b^{(1)} < \Delta$). As shown by the curves, our observations correspond well to a theoretical model for entanglement generation, transfer, and verification (see section 9.14). In comparison to our former work on coherent splitting of a photon[35] in chapter 8, the heralded atomic and photonic W-states $\{\hat{\rho}_W^{(A)}, \hat{\rho}_W^{(\gamma)}\}$ offer qualitatively richer statistical passages through the entanglement spaces delineated by $\{\Delta, y_c\}$. Here, the quantum coherence Δ is intrinsically linked to the statistical character y_c due to quantum correlations between the heralding fields γ_1 and the excitation statistics of the ensembles.

For $\xi \ll 1$, the coherent contribution $\hat{\rho}_c^{(A)}$ of the delocalized single quantum strongly dominates over any other processes for the full quadripartite state $\hat{\rho}_W^{(A)}$ in Eq. 9.3. With a heralding probability $p_h \simeq 3 \times 10^{-4}$ ($\xi \simeq 5 \times 10^{-3}$), we achieve the smallest entanglement parameters $\Delta^{\text{min}} = 0.07^{+0.01}_{-0.02}$ and $y_c^{\text{min}} = 0.038 \pm 0.006$ for the generated quadripartite entangled states. These parameters are suppressed below the closest 3-mode boundary $\Delta_b^{(3)}$ by ten standard deviations. Furthermore, because the local mapping of quantum states from matter to light cannot increase entanglement[27], our measurements of $\hat{\rho}_W^{(\gamma)}$ unambiguously provide a lower bound of the quadripartite entanglement stored in $\hat{\rho}_W^{(A)}$. Therefore, the observed strong violation of the uncertainty relations for $\{\Delta^{\text{min}}, y_c^{\text{min}}\}$ categorically certifies for the creation of measurement-induced entanglement of spin-waves among four quantum memories, as well as for the coherent transfer of the stored quadripartite entangled states to an entangled state of four propagating electromagnetic fields.

In terms of state fidelity, our approach for heralded multipartite entanglement generation compares favorably to matter systems utilizing local interactions (e.g., trapped ions[275,276]). Despite the intrinsically low preparation probability, the resulting quadripartite entangled state $\hat{\rho}_W^{(A)}$ stored in the four ensembles has high fidelity with the ideal W-state, namely $F^{(A)} = {}_A\langle W|\hat{\rho}_W^{(A)}|W\rangle_A$. As discussed in section 9.13.2, we estimate a lower bound for the unconditional entanglement fidelity $F^{(A)} \geq 0.9 \pm 0.1$, as compared to the theoretical fidelity $F_{\text{th}}^{(A)} = 0.98$ derived for the parameters in our experiment.

Apart from the creation of novel multipartite entangled spin-waves, an important benchmark of a quantum interface is the transfer efficiency λ of multipartite entanglement from matter to light[30]. Since no known measure applies to our case, we tentatively define the entanglement transfer $\lambda = F^{(\gamma)}/F^{(A)}$, with physical fidelity $F^{(\gamma)} = {}_\gamma\langle W|\hat{\rho}_W^{(\gamma)}|W\rangle_\gamma$ for the photonic state $\hat{\rho}_W^{(\gamma)}$. In particular for $\xi \ll 1$, we obtain $F_{\text{th}}^{(\gamma)} \simeq$

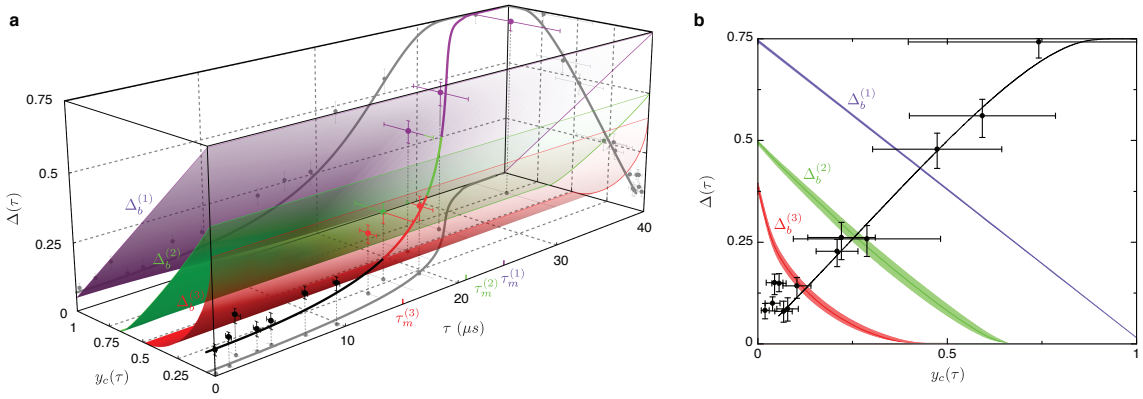

Figure 9.3: **Dissipative dynamics of atomic entanglement. a,** Dynamic evolution of entanglement parameters $\{\Delta(\tau), y_c(\tau)\}$ for the multipartite quantum state. We observe crossing of the boundaries defined by 3-mode (red surface, $\Delta_b^{(3)}$), 2-mode (green surface, $\Delta_b^{(2)}$) entangled states, and separable states (purple surface, $\Delta_b^{(1)}$). We indicate various entanglement orders for quadripartite (black), tripartite (red), bipartite entangled (green) states, and fully separable states (purple) for the data points and the curve. The projections of the data points into the planes (y_c, τ) and (Δ, τ) display the individual passages of $\{\Delta(\tau), y_c(\tau)\}$ (section 9.14.5). **b,** Projection of entanglement dynamics onto the (Δ, y_c) plane. The curves in **a** and **b** are from a theoretical model including motional dephasing. Error bars for the data represent the statistical and systematic uncertainties.

$\eta_{\text{read}} F_{\text{th}}^{(A)}$, which thereby gives $\lambda_{\text{th}} \simeq \eta_{\text{read}} = 38 \pm 4\%$ dictated by the retrieval efficiency η_{read}. While fidelity is an often used measure, we emphasize that $F^{(\gamma)}$ cannot be used to set a threshold for entanglement, since $\hat{\rho}_W^{(\gamma)}$ can exhibit multipartite entanglement for any $F^{(\gamma)} > 0$.

9.5.1 Generation and characterization of a 'crossed' quantum state

As a control experiment, we reconfigured the heralding interferometer such that path-information could in principle be revealed up to the bipartite split of the ensemble pairs $\{a, b\}$ and $\{c, d\}$ by analyzing the polarization state of the heralding photon γ_1. In this case, the heralding measurement $\hat{\Pi}_\times$ prepares a 'crossed' atomic state $\hat{\rho}_\times^{(A)}$ with no coherence shared between $\{a, b\}$ and $\{c, d\}$. Thus, we observe an absence of interference in Fig. 9.2a (orange points). However, this modified $\hat{\Pi}_\times$ preserves the bipartite entanglement within $\{a, b\}$ and $\{c, d\}$, which explains our observation of the uncertainty Δ reduced below the 1-mode bound $\Delta_b^{(1)}$ for $y_c = 0.07 \pm 0.01$. Similarly, we also detect the statistical transition of the bipartite entanglement to fully separable states for the 'crossed' state in Fig. 9.2b, despite the disentanglement for the physical bipartition (|) of $\{a, b\}|\{c, d\}$.

9.6 Dissipative dynamics of atomic entanglement

To investigate the dynamical behavior of the observed quadripartite entangled states, we study the temporal evolution of multipartite entanglement stored in the atomic ensembles as a function of a storage time τ.

Decoherence for the atomic W-state is governed by motional dephasing of spin-waves (ref.[82], chapter 2), in which the imprinted atomic phases in $|\overline{s}_\epsilon\rangle$ evolve independently due to thermal motion, thereby transforming the initial collective state into a subradiant state uncorrelated with the heralding fields γ_1 (section 9.14.5). The net effect is an increase of both entanglement parameters $\{\Delta, y_c\}$ with a time-scale $\tau_m \simeq 17\ \mu s$ (see section 9.9). Eventually, the growth in $\{\Delta(\tau), y_c(\tau)\}$ leads to time-dependent losses of entanglement, marked by successive crossings of the boundaries set by $\{\Delta_b^{(3)}, \Delta_b^{(2)}, \Delta_b^{(1)}\}$.

We examine the dissipative dynamics of multipartite entanglement for the quantum memories of four ensembles via the evolution of both $\{\Delta, y_c\}$ in Fig. 9.3a. We observe the passage of the initial quadripartite entangled state $\hat{\rho}_W^{(A)}(\tau_0)$ at $\tau_0 = 0.2\ \mu s$ through various domains, progressively evolving from M-partite entanglement to $(M-1)$-partite entanglement at memory times $\tau = \tau_m^{(M-1)}$, with the final state $\hat{\rho}_W^{(A)}(\tau_f)$ measured at $\tau_f = 36.2\ \mu$s. The crossings of the bounds $\{\Delta_b^{(3)}, \Delta_b^{(2)}, \Delta_b^{(1)}\}$ occur at $\tau_m^{(3)} = 15\ \mu s$, $\tau_m^{(2)} = 21\ \mu s$, and $\tau_m^{(1)} = 24\ \mu s$, respectively. In addition, the measured entanglement parameters evolve in qualitative agreement to the simulated dynamics derived for $\hat{\rho}_W^{(A)}(\tau)$ from our theoretical model (solid line), with deviations (especially for Δ_{th}) discussed in section 9.14.5. Fig. 9.3b displays the parametric losses of entanglement via $\{\Delta(\tau), y_c(\tau)\}$.

9.7 Thermalization of multipartite entanglement in quantum magnets

Finally, an interesting extension is to relate the characterization of multipartite entanglement via $\{\Delta, y_c\}$ to the relaxations of entanglement in quantum many-body systems[39,40]. We consider two ferromagnetic spin models (Heisenberg-like and Lipkin-Meshkov-Glick Hamiltonians $\hat{H}_{\text{H}}$, $\hat{H}_{\text{LMG}}$) as well as their thermal entanglement $\{\Delta^{(T)}, y_c^{(T)}\}$ (see section 9.15). Results of our analysis are shown in the inset of Fig. 9.2b by the red dashed (blue dash-dotted) lines for the Gibbs thermal equilibrium states $\hat{\rho}_G^{(\text{H})}$ ($\hat{\rho}_G^{(\text{LMG})}$) of $\hat{H}_{\text{H}}$ ($\hat{H}_{\text{LMG}}$). The statistical character of $\hat{\rho}_W^{(A)}$ for our system of four ensembles follows the thermalization of $\hat{\rho}_G^{(\text{H})}$ ($\hat{\rho}_G^{(\text{LMG})}$) for $y_c \lesssim 0.2$, whereby $\hat{\rho}_{\geq 2}^{(A)}$ is thermally populated. This comparison suggests that our method for entanglement characterization could be applied to access the link between off-diagonal long-range order and multipartite entangled spin-waves in thermalized quantum magnets[39,40].

9.8 Conclusion

In conclusion, our measurements explicitly demonstrate a coherent matter-light quantum interface for multipartite entanglement by way of the operational metric of quantum uncertainty relations (refs.[35,38,121], chapters 7–8). High-fidelity entangled spin-waves are generated in four spatially separated atomic ensembles and coherently transferred to quadripartite entangled beams of light. The quantum memories are individually addressable and can be readily read-out at different times for conditional control of entanglement[4], as applied in chapters 3–6. With recent advances by other groups, the short memory times obtained in Fig. 9.3 could be

improved beyond 1 s (section 9.11.1).

Further possibilities include the creation of yet larger multipartite entangled states with efficient scaling[4] for the realization of multipartite quantum networks. For example, quadripartite entangled states of ensemble sets $\{a, b, c, d\}$ and $\{a', b', c', d'\}$ could be extended by swapping between $\{a, a'\}$ to prepare a hexapartite entangled state for $\{b, b', c, c', d, d'\}$ (see section 9.11.1). Generalization of such processes will prepare a single macroscopic entangled state for observing entanglement percolation[6] and extreme non-locality of W-states[289,290], as well as for studying quantum phase transitions in strongly-correlated systems[39,40]. Finally, the entangled spin-waves can be applied for quantum metrology to detect a phase shift of π on an unknown component of $\hat{\rho}_W^{(A)}$ with efficiency beyond any separable state (see section 9.11.2).

9.9 Spin-wave quantum memory

The quantum information of the entangled state for Eq. 9.1 is encoded in the quantum numbers of spin-waves (collective excitations) for the pseudo-spin of the hyperfine ground electronic levels $6S_{1/2}$ ($F = 3, F = 4$) in atomic cesium. The fluorescence images shown in the inset of Fig. 9.1a depict the collective atomic modes of ensembles $\epsilon = \{a, b, c, d\}$ for exciting the entangled spin-waves $\hat{\rho}_W^{(A)}$ with 1 mm separations and 60 μm waists. The geometry of the collective excitations for the four ensembles $\{a, b, c, d\}$ is defined by the point-spread functions of the imaging systems for the fields $\{\gamma_1, \gamma_2\}$, within a cold cloud of $N_{A,\epsilon} \approx 10^6$ cesium atoms (chapter 2). We use an off-axial configuration[75] for individually addressing each ensemble ϵ with an angle $\theta = 2.5^\circ$ between the classical and nonclassical beams (section 9.12.1), that creates spin-waves $|\overline{s}_\epsilon\rangle$ associated with wave-numbers $\delta\vec{k} = \vec{k}_{\text{write}} - \vec{k}_{\gamma_1}$ for each ϵ. These spin-waves are analogous to other types of collective excitations in many-body systems, such as magnons and plasmons, and the spin-waves can be converted to dark-state polaritons for the coherent transfer $\hat{U}_{\text{read}}$ of entanglement (chapter 2). For the phase-matching configuration and temperature of our ensembles, the memory times $\{\tau_m^{(3)}, \tau_m^{(2)}, \tau_m^{(1)}\}$ in Fig. 9.3 are dominantly determined by the motional dephasing of the spin-waves $|\overline{s}_\epsilon\rangle$ (ref.[82], chapter 2). With thermal velocity of $v_t \simeq 14$ cm/s, we estimate a memory time $\tau_m \simeq \frac{0.85\,\mu m}{4\pi \sin(\theta/2) v_t} = 17\ \mu s$. On the other hand, the ground-state dephasing due to inhomogeneous broadening is expected to be $> 50\ \mu s$ in our experiment, inferred from two-photon Raman spectroscopy (chapter 2).

9.10 Operating the quantum interface

For the quantum interface to function during the 3 ms window, in step (1) 20-ns writing (red-detuned $\delta = 10$ MHz from $|g\rangle - |e\rangle$ transition) and 100-ns repumping (resonant with $|s\rangle - |e\rangle$) pulses are applied sequentially to the ensembles ϵ, synchronized to a clock running at $R_c \simeq 2$ MHz. This process creates pairwise correlated excitations[4] between the collective atomic modes $|\overline{s}_\epsilon\rangle$ of the ensembles ϵ and the optical fields γ_1 ($\delta = 10$ MHz below $|s\rangle - |e\rangle$). Photodetection of a single photon for the combined fields γ_1 at the output

of the heralding interferometer effectively erases the which-path information for γ_1, and imprints the entangled spin-wave $\hat{\rho}_W^{(A)}$ (Eq. 9.3) onto the ensembles $\{a, b, c, d\}$ via $\mathrm{Tr}_h(\hat{\Pi}_h \hat{U}_{\text{write}}^{\dagger} \hat{\rho}_g^{(A)} \hat{U}_{\text{write}})$. The heralding event at D_h triggers control logic in Fig. 9.1a which deactivates intensity modulators of the writing (IM_{write}), repumping and reading lasers (IM_{read}) for the quantum storage of $\hat{\rho}_W^{(A)}$ in step (2). After a user-controlled delay τ, step (3) is initiated with 20-ns-strong read pulses (Rabi frequency 24 MHz, resonant with $|s\rangle - |e\rangle$) that address the ensembles in Fig. 9.1c and coherently transfer the entangled atomic components $\{a, b, c, d\}$ of $\hat{\rho}_W^{(A)}(\tau)$ one-by-one to propagating beams $\gamma_2 = \{a_2, b_2, c_2, d_2\}$, comprising the entangled photonic state $\hat{\rho}_W^{(\gamma)}(\tau)$, via the operation $\hat{\rho}_W^{(\gamma)} = \mathrm{Tr}_A(\hat{U}_{\text{read}}^{\dagger} \hat{\rho}_W^{(A)} \hat{U}_{\text{read}})$. Here, Tr_A traces over the atomic systems which are later shelved into the ground states $|\overline{g}_\epsilon\rangle$. The retrieval efficiency η_{read} is collectively enhanced for large N_A (ref.[4]), leading to $\eta_{\text{read}} = 0.38 \pm 0.06$ in our experiment. The average production rate for the atomic quadripartite entanglement with $\{\Delta^{\min}, y_c^{\min}\}$ is $r_p = R_c D_c p_h \simeq 60$ Hz, while the actual rate during the 3 ms operating window is $r_q = R_c p_h \simeq 500$ Hz. The atomic level diagrams for entanglement generation and quantum-state exchanges are shown as insets to Figs. 9.1b and 9.1c. States $|g\rangle$, $|s\rangle$ are hyperfine ground states $F = 4$, $F = 3$ of $6S_{1/2}$ in atomic cesium; state $|e\rangle$ is the hyperfine level $F' = 4$ of the electronic excited state $6P_{3/2}$.

9.11 Prospects and discussion

9.11.1 Improving memory time and matter-light transfer efficiency

By operating the clock speed at $R_c \to 10$ MHz and $\tau_m^{(3)} \approx 20\ \mu s$, we could prepare hexapartite ($M = 6$) entanglement with probability $3z\eta_{\text{read}} p_h^2/8 \approx 10^{-5}$ by connecting two quadripartite states $\hat{\rho}_W^{(A)}$ for $\{\Delta^{\min}, y_c^{\min}\}$, with enhancement factor $z = 400$ (ref.[36]), thereby giving a local production rate of $r_q \approx 50 - 100$ Hz, or an average rate $r_p \approx 5 - 10$ Hz with our current duty cycle D_c. The most challenging aspect of verifying the hexapartite entangled states is the quantification of the higher-order contamination $\hat{\rho}_{\geq 2}$, which we estimate ~ 1 event per 10 hr. This integration rate is feasible with our current system. More generally, M_1 and M_2-partite entangled states can be fused together by entanglement connection to create a $M = (M_1 + M_2 - 2)$-partite entangled state. However, the memory times $\{\tau_m^{(3)}, \tau_m^{(2)}, \tau_m^{(1)}\}$ in Fig. 9.3 and the entanglement transfer λ from matter to light limit our capability to scale the multipartite entanglement beyond $M > 6$ by way of conditional control and connection of entanglement[36,37] with our current experimental parameters (chapters 4–5).

The prerequisite storage techniques for suppressing both the internal and motional spin-wave dephasings can be extended for τ_m with advances in ensemble-based quantum memories[48,114,115]. Recent experiments with single ensembles have achieved coherence times up to $\tau_m \simeq 1.5$ seconds in quantum degenerate gases[116,117] albeit with efficiencies $\lesssim 1\%$. The transfer efficiency can also be increased to $\lambda_{\text{th}} \simeq 0.9$ by enclosing the ensembles with high finesse cavities[82]. System integrations by way of atom-chip technology

and waveguide coupling [133,291] hold great potential for scalability given the strong cooperativity and the long coherence [292]. At this level, two or more heralded processes of multipartite entanglement generations can be made 'on-demand' on time scales of $\tau_{\text{det}} \sim \frac{1}{R_c p_h} = 1$ ms, with $\tau_m \gg \tau_{\text{det}}$ (refs. [36,37], chapters 4–5).

Realistically, the expansion of multipartite entangled states $\hat{\rho}_W^{(A)}$ will be limited by the intrinsic degradations of the entanglement parameters $\{\Delta, y_c\}$, that inevitably increase with each step of entanglement connection (ref. [37], chapter 5), and by the specific quantum repeater architecture implemented on $\hat{\rho}_W^{(A)}$. The latter is an extremely rich area of research in view of the large classes of methods for connecting multipartite entangled states, making it premature to specify a particular architecture for multipartite entanglement expansion. However, our experiment will hopefully stimulate theoretical studies of complex repeater architectures for multipartite systems, beyond traditional one-to-one networks [49].

9.11.2 Quantum-enhanced parameter estimation with entangled spin-waves

We describe a quantum-enhanced parameter estimation protocol whereby a phase shift on a single ensemble ϵ_i of the quadripartite state $\epsilon_i \in \{a, b, c, d\}$ can be detected with efficiency beyond that for any separable state. Specifically, we consider a π-phase shift $\hat{U}_{\pi,\epsilon_i} = \exp(i\pi\hat{n}_{\epsilon_i})$ applied on an unknown spin-wave component $\epsilon_i \in \{a, b, c, d\}$ ($\hat{n}_{\epsilon_i} = \hat{S}_{\epsilon_i}^{\dagger}\hat{S}_{\epsilon_i}$) of the atomic state $\hat{\rho}_W^{(A)}$, or on a spatial field mode $\gamma_{2i} \in \{a_2, b_2, c_2, d_2\}$ of the photonic state $\hat{\rho}_W^{(\gamma)}$ ($\hat{n}_{\gamma_{2i}} = \hat{a}_{\gamma_{2i}}^{\dagger}\hat{a}_{\gamma_{2i}}$). Our goal is to find the π-phase shifted ensemble ϵ_i (optical mode γ_{2i}), in a *single-measurement* under the condition that an average of one spin-wave is populated in total; i.e., $\sum_i \text{Tr}(\hat{n}_{\epsilon_i}\hat{\rho}_W^{(A)}) = 1$ (or $\sum_i \text{Tr}(\hat{n}_{\gamma_{2i}}\hat{\rho}_W^{(\gamma)}) = 1$ for optical modes). As a quantum benchmark, we consider an average success probability $P_s = \frac{1}{4}\sum_{\epsilon_i} \text{Tr}(\hat{\Pi}_{\epsilon_i}^{(u)}\hat{U}_{\pi,\epsilon_i}^{\dagger}\hat{\rho}_W^{(A)}\hat{U}_{\pi,\epsilon_i})$ (failure probability $P_f = 1 - P_s$) for distinguishing the phase-shifted ensemble ϵ_i (mode γ_{2i}) among the four possibilities $\{a, b, c, d\}$ ($\{a_2, b_2, c_2, d_2\}$) by way of *unambiguous quantum-state discrimination* $\{\hat{\Pi}_{\epsilon_i}^{(u)}\}$ (refs. [293–296]).

First, we consider an ideal W-state $|W\rangle_o = |W\rangle_A$ (or $|W\rangle_{\gamma_2}$) with atomic phases $\phi_i \in \{\phi_1, \phi_2, \phi_3\}$ (photonic phases $\phi_i' \in \{\phi_1', \phi_2', \phi_3'\}$). In this case, the π-phase shifted entangled W-states

$$|W_{\epsilon_i}\rangle_f \in \{|W_a^{(\pi)}\rangle_f, |W_b^{(\pi)}\rangle_f, |W_c^{(\pi)}\rangle_f, |W_d^{(\pi)}\rangle_f\}$$

can be detected deterministically, because $|W_{\epsilon_i}^{(\pi)}\rangle_f = \hat{U}_{\pi,\epsilon_i}|W\rangle_o$ forms an orthonormal complete set that spans the state-space $\hat{\rho}_1$, resulting from the underlying symmetry of $|W\rangle_o$ with respect to any rotation $\hat{U}_{\pi,\epsilon_i}$ on a generalized Bloch sphere. Operationally, we set the verification phases $\beta_{1,2} - \phi_{1,2}' = 0$ and $\beta_3 - \phi_3' = \pi$. Then, the π-phase shifted ensemble ϵ_i can be unambiguously discriminated because the otherwise balanced output photon probabilities $\vec{p}_v = \{p_{1000}, p_{0100}, p_{0010}, p_{0001}\} = \{0.25, 0.25, 0.25, 0.25\}$ of the verification interferometer will be transformed to $\vec{p}_v = \{1, 0, 0, 0\}$ for a π-phase induced on ensemble a, to $\vec{p}_v = \{0, 1, 0, 0\}$ on ensemble b, to $\vec{p}_v = \{0, 0, 1, 0\}$ on ensemble c, and to $\vec{p}_v = \{0, 0, 0, 1\}$ on ensemble d, each with success probability $P_s^{(\text{ent})} = 1$.

For fully separable states $|\Psi\rangle_o = |\psi_a\rangle_a|\psi_b\rangle_b|\psi_c\rangle_c|\psi_d\rangle_d$ with $|\psi_{\epsilon_i}\rangle_{\epsilon_i} = \sum_{n=0}^{\infty} c_{\epsilon_i}^{(n)}|n\rangle_{\epsilon_i}$, we displace

the resulting π-phase shifted state $|\Psi_{\epsilon_i}^{(\pi)}\rangle_f = \hat{U}_{\pi,\epsilon_i}|\Psi\rangle_o$ with a local unitary transformation $\hat{V}_{\epsilon_i}|\psi_{\epsilon_i}\rangle_{\epsilon_i} = |0\rangle_{\epsilon_i}$. The overall process $\hat{V}_a\hat{V}_b\hat{V}_c\hat{V}_d\hat{U}_{\pi,\epsilon_i}$ maps the initial product state $|\Psi\rangle_o$ into $\hat{V}_a\hat{U}_{\pi,a}|\psi_a\rangle_a|0\rangle_b|0\rangle_c|0\rangle_d$ (a phase shift on ensemble a), $|0\rangle_a\hat{V}_b\hat{U}_{\pi,b}|\psi_b\rangle_b|0\rangle_c|0\rangle_d$ (ensemble b), $|0\rangle_a|0\rangle_b\hat{V}_c\hat{U}_{\pi,c}|\psi_c\rangle_c|0\rangle_d$ (ensemble c), and $|0\rangle_a|0\rangle_b|0\rangle_c\hat{V}_d\hat{U}_{\pi,d}|\psi_d\rangle_d$ (ensemble d), with only one ϵ_i containing $\langle\hat{n}_{\epsilon_i}\rangle > 0$ excitations. Thus, we can *unambiguously* identify the phase-shifted ensemble ϵ_i given a photodetection, albeit with a failure probability $P_f = \frac{1}{4}\sum_{\epsilon_i}|_{\epsilon_i}\langle 0|\hat{V}_{\epsilon_i}\hat{U}_{\pi,\epsilon_i}|\psi_{\epsilon_i}\rangle_{\epsilon_i}|^2 = \frac{1}{4}\sum_{\epsilon_i}|_{\epsilon_i}\langle\psi_{\epsilon_i}|\hat{U}_{\pi,\epsilon_i}|\psi_{\epsilon_i}\rangle_{\epsilon_i}|^2$ arising from *inconclusive* null events (i.e., $|0000\rangle\langle 0000|$). We derive the maximum success probability $P_s^{(\max)} = 1 - P_f^{(\min)}$ and the optimal state $|\Psi\rangle_o = |\Psi\rangle_{\text{opt}}$ by minimizing $P_f^{(\min)}$ over all possible realizations of $c_{\epsilon_i}^{(n)}$ satisfying $\sum_{\epsilon_i}\langle\psi_{\epsilon_i}|\hat{n}_{\epsilon_i}|\psi_{\epsilon_i}\rangle_{\epsilon_i} = 1$. Specifically, we find that an optimal (pure) separable state $|\Psi\rangle_{\text{opt}} = \prod_{\epsilon_i}(\sqrt{3/4}|0\rangle_{\epsilon_i} + \sqrt{1/4}|1\rangle_{\epsilon_i})$ can be used for the parameter estimation protocol to infer ϵ_i with $P_s^{(\max)} = 0.75$. Similarly, maximum success probability $P_s^{(\text{coh})}$ can be derived for multimode coherent states $\prod_{\epsilon_i}|\alpha_{\epsilon_i}\rangle_{\epsilon_i}$, giving a classical bound of $P_s^{(\text{coh})} = 1 - 1/e$.

Finally, we consider the upper bound $P_s^{(\max)}$ for mixed separable states $\hat{\rho}_o^{(\text{sep})}$ with pure state decompositions $\hat{\rho}_o^{(\text{sep})} = \sum_m p_m|\Psi_m\rangle_o\langle\Psi_m|$. Generally, the transformations $\hat{V}_{\epsilon_i}$, as discussed above, do not exist for $\hat{\rho}_o^{(\text{sep})}$, excluding the possibility of an unambiguous state discrimination. Thus, the success probability $P_s(\hat{\rho}_o^{(\text{sep})})$ is upper bounded by the convex combinations of $\{|\Psi_m\rangle\}$, thereby

$$P_s(\hat{\rho}_o^{(\text{sep})}) \leq \sum_m p_m P_s(|\Psi_m\rangle_o\langle\Psi_m|) \leq P_s^{(\max)} = 0.75. \tag{9.4}$$

Importantly, the maximum success probability $P_s^{(\max)} = 0.75$, attainable for any $\hat{\rho}_o^{(\text{sep})}$, is less than $P_s^{(\text{ent})} = 1$ for entangled states $|W\rangle_o$. Thus, the entangled spin-waves in the experiment can be applied for sensing an atomic phase shift beyond the limit for any unentangled state.

9.12 Experimental details

The experiment consists of a 22 ms preparation stage and a 3 ms period for operating the quantum interface in Fig. 9.1 with a repetition rate 40 Hz and a duty cycle $D_c = 3/25$. For the preparation, we load and laser-cool cesium atoms (peak optical depth ≈ 30) in a magneto-optical trap for 18 ms, after which the atoms are released from the trap with dynamically compensated eddy-currents. The atoms are further cooled in an optical molasses ($T_t \simeq 150\ \mu K$) for 3.8 ms, and optically pumped to $|g\rangle$ for 0.2 ms. During this time, a phase-reference laser ($F = 3 \leftrightarrow F' = 4'$ transition) also propagates through the atomic ensembles for the active stabilization of the verification interferometer in Fig. 9.1c via *ex-situ* phase-modulation spectroscopy[35], which does not affect the operation of the quantum interface (section 9.12.2). Concurrently, dense cesium atoms in paraffin coated vapor cells located at the heralding and verification ports are prepared to the respective ground states $|g\rangle$ ($|s\rangle$) for filtering the coherent-state lasers scattered into the quantum fields γ_1 (γ_2).

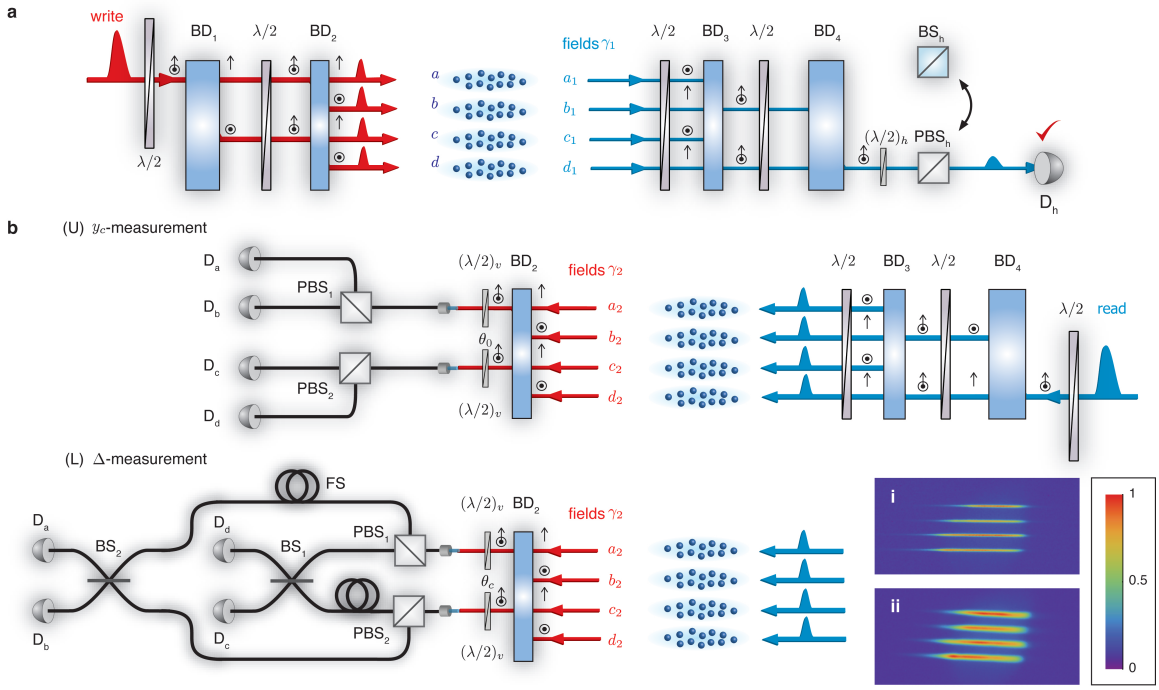

Figure 9.4: **Experimental schematics for entanglement generation, transfer, and verification. a,** Entanglement generation. A weak write laser is sequentially split into four components by displacers $\{\mathrm{BD}_1, \mathrm{BD}_2\}$ to excite atomic ensembles $\epsilon = \{a, b, c, d\}$. The resulting fields $\gamma_1 = \{a_1, b_1, c_1, d_1\}$ are brought into interferences with displacer BD_4 and polarizing beamsplitter PBS_h, and sent to a single-photon detector D_h. A detection event at D_h heralds the creation of a quadripartite entangled state. **b,** Quantum-state transfer and entanglement verification. After a storage time τ, we convert the atomic state of the ensembles $\epsilon = \{a, b, c, d\}$ to an entangled state for fields $\gamma_2 = \{a_2, b_2, c_2, d_2\}$ by way of strong read pulses. (U) y_c-measurement—By setting the waveplates $(\lambda/2)_v$ to $\theta_0 = 0°$, we measure the occupation statistics of the individual modes with detectors $D_{a,b,c,d}$. (L) Δ-measurement—With $(\lambda/2)_v$ at $\theta_c = 22.5°$, we optimize the verification phases $\{\beta_1, \beta_2, \beta_3\}_v$ for constructive interferences of the fields γ_2 at $\mathrm{PBS}_{1,2}$ and $\mathrm{BS}_{1,2}$. Piezoelectric fiber stretching modules (FS) are used in the verification interferometer for active stabilizations of $\{\beta_1, \beta_2, \beta_3\}_v$. The quadripartite atomic entanglement is generated for four collective atomic modes of the ensembles $\epsilon = \{a, b, c, d\}$ in inset (i), which are individually controlled by the classical writing, repumping, and reading lasers, whose fluorescence is shown in inset (ii). Both images in the insets (i), (ii) result from background-subtracted fluorescences of the four atomic ensembles. The quantum fields $\{\gamma_1, \gamma_2\}$ are generated in a non-collinear geometry[75] with a crossing angle of 2.5° (not shown) relative to the classical beams (chapter 2).

9.12.1 Experimental procedures for matter-light quantum interface

As shown in Fig. 9.4a, we split a write pulse into four beams with two calcite beam-displacers $\{\mathrm{BD}_1, \mathrm{BD}_2\}$, with output fields of the form $\vec{E}_{\text{write}} = (\vec{E}_a + e^{i\phi_1^{(w)}}\vec{E}_b) + e^{i\phi_2^{(w)}}(\vec{E}_c + e^{i\phi_3^{(w)}}\vec{E}_d)$. We control their relative intensities using the two waveplates $(\lambda/2)$ near $\{\mathrm{BD}_1, \mathrm{BD}_2\}$, with writing phases $\phi_i^{(w)} \in \{\phi_1^{(w)}, \phi_2^{(w)}, \phi_3^{(w)}\}$ set by the tilting angles of $\{\mathrm{BD}_1, \mathrm{BD}_2\}$. In turn, the heralding fields $\gamma_1 = \{a_1, b_1, c_1, d_1\}$ emitted from the writing process are combined into two spatial modes at BD_3, with each mode carrying polarizations $\{|H\rangle, |V\rangle\}$ to accommodate the fields $\gamma_1^{(ab)} = \{a_1, b_1\}$ and $\gamma_1^{(cd)} = \{c_1, d_1\}$. We then interfere the polarization components of the spatial modes $\{\gamma_1^{(ab)}, \gamma_1^{(cd)}\}$ by way of BD_4, whose output modes experience

polarization interference at the polarizing beamsplitter PBS_h, with one output monitored by the heralding detector D_h. Here, the relative phases acquired by the propagation of fields γ_1 before the detection at D_h are given by $\phi_i^{(h)} \in \{\phi_1^{(h)}, \phi_2^{(h)}, \phi_3^{(h)}\}$. We control $\phi_i^{(h)}$ with a set of Berek compensators.

A photoelectric detection of a single photon γ_1 emitted indistinguishably by one of four ensembles $\epsilon = \{a, b, c, d\}$ prepares an atomic entangled state $\hat{\rho}_W^{(A)}$, whose mutual phases $\phi_i \in \{\phi_1, \phi_2, \phi_3\}$ between ensembles $\{a, b\}$, $\{a, c\}$, and $\{c, d\}$ are $\phi_i = \phi_i^{(w)} - \phi_i^{(h)}$ for $i \in \{1, 2, 3\}$. To generate a 'crossed' quantum state $\hat{\rho}_\times^{(A)}$, we replace PBS_h with a non-polarizing beamsplitter BS_h in the heralding interferometer (Fig. 9.4a), such that the fields $\gamma_1^{(ab)}$ and $\gamma_1^{(cd)}$ are mixed with orthogonal polarizations. While in practice we do not discriminate events arising from the fields $\gamma_1^{(ab)}$ and $\gamma_1^{(cd)}$, the intrinsic possibility of analyzing the polarization state of the heralding photon to infer the two distinct events completely destroys the bipartite coherence (and entanglement) for the split between $\{a, b\}$ and $\{c, d\}$.

Finally, after a variable delay, a strong counter-propagating read pulse, with reading phases $\phi_i^{(r)} \in \{\phi_1^{(r)}, \phi_2^{(r)}, \phi_3^{(r)}\}$ set by $\{\mathrm{BD}_3, \mathrm{BD}_4\}$, transforms the entangled atomic components $\{a, b, c, d\}$ of $\hat{\rho}_W^{(A)}$ to entangled beams $\gamma_2 = \{a_2, b_2, c_2, d_2\}$ comprising the photonic state $\hat{\rho}_W^{(\gamma)}$. The photonic phases $\{\phi_1', \phi_2', \phi_3'\}$ of $\hat{\rho}_W^{(\gamma)}$ depend on the overall accumulation of atomic phases ϕ_i via $\phi_i' = \phi_i^{(r)} - \phi_i$. Importantly, the set of calcite displacers $\{\mathrm{BD}_1, \mathrm{BD}_2, \mathrm{BD}_3, \mathrm{BD}_4\}$ forms an interferometrically stable four-mode Mach-Zehnder device, in which any common-mode phase drift of $\{\phi_i^{(w)}, \phi_i^{(r)}, \phi_i^{(h)}, \phi_i'\}$ is passively counter-balanced over several days. Thus, the entangled state $\hat{\rho}_W^{(A)}$ ($\hat{\rho}_W^{(\gamma)}$) in our experiment is generated with stable phases $\{\phi_1, \phi_2, \phi_3\}$ ($\{\phi_1', \phi_2', \phi_3'\}$) from trial to trial, which can be transferred to independent reference frames for entanglement verification without exploiting additional quantum channels [110].

9.12.2 Operational procedures for entanglement verification

To verify the entanglement of the photonic state $\hat{\rho}_W^{(\gamma)}$, we use a nonlocal, nonlinear uncertainty relation (ref. [38], chapter 7), in which mode-entangled states for $M > 2$ can be efficiently detected with a significantly smaller number of measurements than conventional techniques [35,38], as discussed in chapters 7–8. Specifically, our protocol requires measurements of (U) the photon statistics y_c and (L) the mutual coherences Δ of the multipartite entangled optical modes, as shown in Fig. 9.4b.

Operationally, we measure the entanglement parameters by first combining the four optical modes $\gamma_2 = \{a_2, b_2, c_2, d_2\}$ with BD_2 into two spatial modes $\gamma_2^{(ab)} = \{a_2, b_2\}$ and $\gamma_2^{(cd)} = \{c_2, d_2\}$, with each mode $\{a_2, b_2\}$ ($\{c_2, d_2\}$) of γ_2 encoded in the respective polarizations $\{|H\rangle, |V\rangle\}$ of $\gamma_2^{(ab)}$ ($\gamma_2^{(cd)}$). By rotating two waveplates $(\lambda/2)_v$ before $\mathrm{PBS}_{1,2}$ between $\theta_0 = 0^\circ$ and $\theta_c = 22.5^\circ$, and by reconfiguring the fiber-optical connections, we switch between the measurement setups for accessing y_c and Δ.

In particular, measuring the sum uncertainty Δ involves pairwise interference of the optical channels $\gamma_2 = \{a_2, b_2, c_2, d_2\}$. The coherence properties of the photonic state are characterized by the stable photonic phases of $\{\phi_1', \phi_2', \phi_3'\}$, and by the off-diagonal elements $d_{\alpha\beta}$ of $\hat{\rho}_W^{(\gamma)}$ (section 9.13.1). This requires high phase stability of $\{\beta_1, \beta_2, \beta_3\}_v$ for the relative optical paths of the verification interferometer shown in Fig.

9.4b. Here, $\{\beta_1, \beta_2, \beta_3\}_v$ denote to the relative phases between the modes $\{a_2, b_2\}$, $\{a_2, c_2\}$, and $\{c_2, d_2\}$, respectively. Additionally, $\{\beta_1, \beta_2, \beta_3\}_v$ of each optical path leading from the output faces of the ensembles must be tuned to $\{\phi_1', \phi_2', \phi_3'\}$ such that maximum constructive interferences for the fields $\{a_2, b_2, c_2, d_2\}$ occur in a pairwise and sequential fashion (ref.[35], see a similar setup in section 8.8.2). We achieve the optimal settings of these phases by varying $\{\beta_1, \beta_2, \beta_3\}_v$ and recording the sum uncertainty. Fig. 9.2a shows such a measurement for β_2.

To stabilize the verification phases $\{\beta_1, \beta_2, \beta_3\}_v$, we incorporated an auxiliary reference laser $\vec{E}_{\text{aux}}$ to probe the interferometer during the laser cooling and trapping stage of our experiment via an *ex-situ* phase modulation spectroscopy. The active stabilizations of $\{\beta_1, \beta_2, \beta_3\}_v$ rely upon the passively stable paths of the eight quantum fields $\{\gamma_1, \gamma_2\}$.

During the phase stabilization stage, the outputs of the verification interferometer are routed to a set of auxiliary photodetectors by micro-electro-mechanical switches (MEMS) to monitor $\{\beta_1, \beta_2, \beta_3\}_v$. We also use another set of MEMS for switching $\vec{E}_{\text{aux}}$, which can extinguish the intensity of the reference laser with an overall extinction of $\gtrsim 200$ dB during the operation of the quantum interface. Additionally, by setting the frequency of $\vec{E}_{\text{aux}}$ to the $|s\rangle - |e\rangle$ transition of cesium, $\vec{E}_{\text{aux}}$ initializes the ensembles $\epsilon = \{a, b, c, d\}$ to the ground state $|g\rangle$ of the quantum interface. Based on the interference signal of $\vec{E}_{\text{aux}}$, we apply a feedback signal to the two piezoelectric fiber stretching modules (FS) in Fig. 9.4 that control the relative path lengths (β_2) leading from the ensembles. The remaining phases $\{\beta_1, \beta_3\}_v$ are passively stabilized by stable interferometers (over several days), and controlled independently with a set of calcite Berek compensators.

To operate the quantum interface (3 ms), (i) we set the control signals for the fiber stretchers to values $V_0 + V_c$, with set-point V_0 corresponding to a fixed phase β_2 of the interferometer during stabilization, (ii) switch off the laser $\vec{E}_{\text{aux}}$, and (iii) reroute the interferometer outputs to the single-photon counters $D_{a,b,c,d}$ via the MEMS for 3 ms. This system allows to set the phase β_2 to an arbitrary value by incrementing V_0 by V_c to $V_0 + V_c$, with no degradation for the quantum statistics and coherence of $\hat{\rho}_W^{(\gamma)}$. Moreover, the verification phases remain stable for the 3-ms operating duration of the quantum interface. Thus, the asynchronous (*'ex-situ'*) sequences for acquiring and stabilizing $\{\beta_1, \beta_2, \beta_3\}_v$ of the verification interferometer do not affect the sensitive operation of the quantum interface. In addition, the asynchronous timings allow the generation process of the atomic (photonic) entanglement with atomic (photonic) phases $\{\phi_1, \phi_2, \phi_3\}$ ($\{\phi_1', \phi_2', \phi_3'\}$) to be independent of the procedures for stabilizing the verification phases $\{\beta_1, \beta_2, \beta_3\}_v$, thereby satisfying the entanglement verification criteria of ref.[110].

9.13 Quantum uncertainty relations and genuine multipartite entanglement

In order to verify the entanglement by way of $\{\Delta, y_c\}$, we first evaluate the photon statistics $\{p_0, p_1, p_{\geq 2}\}$ for the y_c-measurement. Operationally, this is accomplished by measuring the individual probabilities q_{ijkl} for $i, j, k, l \in \{0, 1\}$ photons to occupy the respective optical modes $\gamma_2 = \{a_2, b_2, c_2, d_2\}$ at the output faces of the ensembles via photoelectric detections $\{\hat{\Pi}_i^{(s)}\}$. For the Δ-measurement, we quantify the off-diagonal coherence $\overline{d}$ of $\hat{\rho}_W^{(\gamma)}$ by pairwise interferences of all possible sets of modes $\alpha, \beta \in \{a_2, b_2, c_2, d_2\}$ with the verification interferometer. The photon probabilities $\{p_{1000}, p_{0100}, p_{0010}, p_{0001}\}$ at the output modes of the verification interferometer thereby result from the coherent interferences of the four purportedly entangled fields γ_2 that depend on the phase orientations $\{\beta_1, \beta_2, \beta_3\}_v$ of $\{\hat{\Pi}_i^{(c)}\}$ (section 9.12.2).

Our conclusion of genuine multipartite entanglement for the atomic and photonic states $\{\hat{\rho}_W^{(A)}, \hat{\rho}_W^{(\gamma)}\}$ does not rely on weaker conditions based on the non-separability along any fixed bipartition of $\{\hat{\rho}_W^{(A)}, \hat{\rho}_W^{(\gamma)}\}$. The genuine M-partite entangled states created from our experiment can only be represented as mixtures of pure states that *all* possess M-partite entanglement, as for the case of genuine 'k-producibility' in multipartite spin models[39,40]. We take caution that our entanglement verification protocol cannot be applied for verifying the *absence* of entanglement for the physical state $\hat{\rho}_W^{(\gamma)}$ in an infinite dimension[206]. Finally, we emphasize that our analysis makes use of the full physical state $\{\hat{\rho}_W^{(A)}, \hat{\rho}_W^{(\gamma)}\}$ including the vacuum component $\hat{\rho}_0$ and higher-order terms $\hat{\rho}_{\geq 2}$, and does not rely on a spurious *post-diction* based upon a preferred set of detection events (see sections 9.13.3–9.13.4).

In the following, I will derive useful relationships between the entanglement witness by way of quantum uncertainty relations and other measures.

9.13.1 Relationship between quantum uncertainty and off-diagonal coherences

We derive here the general expression for the upper bound of the sum uncertainty Δ as a function of the coherence $\overline{d}$. First, we note that Δ is only sensitive to the 1-excitation subspace $\hat{\rho}_1$ of $\hat{\rho}_r$ with

$$\hat{\rho}_1 = \begin{pmatrix} s_{1000} & d_{ab} & d_{ac} & d_{ad} \\ d_{ba}^* & s_{0100} & d_{bc} & d_{bd} \\ d_{ca}^* & d_{cb}^* & s_{0010} & d_{cd} \\ d_{da}^* & d_{db}^* & d_{dc}^* & s_{0001} \end{pmatrix},$$

normalized such that $\mathrm{Tr}(\hat{\rho}_1) = s_{1000} + s_{0100} + s_{0010} + s_{0001} = 1$. Here, the diagonal elements $\vec{s}_1 = \{s_{1000}, s_{0100}, s_{0010}, s_{0001}\}$ of $\hat{\rho}_1$ are related to the 1-photon probabilities $\vec{q}_1 = \{q_{1000}, q_{0100}, q_{0010}, q_{0001}\}$ at the faces of the ensembles via $p_1 \vec{s}_1 = \vec{q}_1$. By transforming $\hat{\rho}_1$ into the basis spanned by $\{|W_i\rangle_v\}$, we find the expressions for the normalized output photon probabilities $\{p_{1000}, p_{0100}, p_{0010}, p_{0001}\}$ of the verification

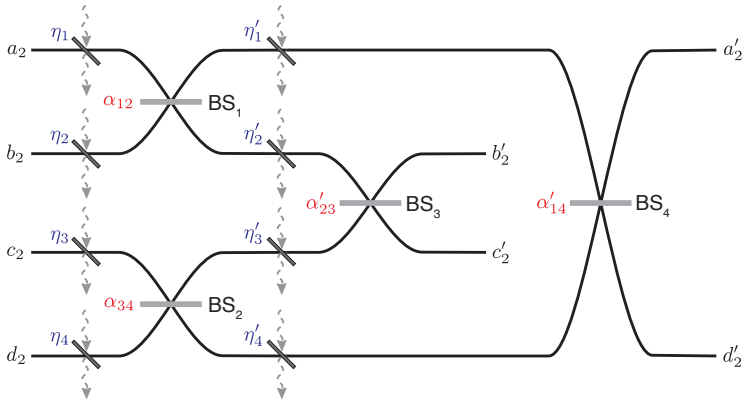

Figure 9.5: **Various imperfections in verification interferometer.** The verification interferometer transforms the input photonic modes $\gamma_2 = \{a_2, b_2, c_2, d_2\}$ to the output modes $\gamma'_2 = \{a'_2, b'_2, c'_2, d'_2\}$. The projectors $\hat{\Pi}_i^{(c)}$ are transformed into imbalanced states $\hat{\pi}_i^{(c)}$ due to losses and imbalances in the verification protocol. The transmission efficiencies $\{\eta, \eta'\}$ (blue) and beamsplitting ratios $\{\alpha, \alpha'\}$ (red) are shown. Dashed arrows are the auxiliary modes for loss propagations of the input state $\hat{\rho}_W^{(\gamma)}$.

interferometer as functions of $\vec{s}_1$ and $d_{\alpha\beta}$. The sum uncertainty Δ is then expressed as $\Delta = \frac{3}{4} - \{(|d_{ab}| + |d_{cd}|)^2 + (|d_{ac}| + |d_{bd}|)^2 + (|d_{ad}| + |d_{bc}|)^2\}$. Thus, we obtain $\Delta \lesssim \frac{3}{4}(1 - 16\overline{d}^2)$. The average value of the six unique off-diagonal elements is $\overline{d} = \frac{1}{6}\sum_{\alpha,\beta} |d_{\alpha\beta}|$ with $0 \leq \overline{d} \leq 1/4$, and the effective interference visibility is given by $V_{\text{eff}} = 4\overline{d}$.

9.13.2 Derivation of entanglement fidelity

We obtain here the expression for the lower bound unconditional entanglement fidelity $F^{(A)} = \tilde{p}_1 F_1$, where $\tilde{p}_1$ is the probability for a single spin-wave $\hat{\rho}_1^{(A)}$ in the heralded state $\hat{\rho}_W^{(A)}$, and $F_1 = \langle W_1|\hat{\rho}_1^{(A)}|W_1\rangle$ is the conditional fidelity for $\hat{\rho}_1^{(A)}$. We start by noting that the projective measurement $\hat{\Pi}_i^{(c)}$ for Δ gives the conditional fidelity F_1 of $\hat{\rho}_r$ onto one of four orthonormal W-states, $|W_i\rangle_v = |W_1\rangle_v$, for example, $|1000\rangle + e^{i\beta_1}|0100\rangle + e^{i\beta_2}(|0010\rangle + e^{i\beta_3}|0001\rangle)$. Hence, we can define $\Delta = 1 - F_1^2 - \sum_{i=2}^4 F_i^2$ in terms of the respective overlaps F_i. Because of the orthonormality $\sum_{i=1}^4 F_i = 1$, the sum uncertainty is bounded by $\Delta \geq 1 - F_1^2 - (1 - F_1)^2$, whereby we obtain $F_1 \geq \sqrt{\frac{1}{2}(\frac{1}{2} - \Delta)} + \frac{1}{2}$. Finally, by combining the probability $\tilde{p}_1$ for exciting one spin-wave distributed among the four ensembles, we access the lower bound fidelity $F^{(A)} \geq \tilde{p}_1(\sqrt{\frac{1}{2}(\frac{1}{2} - \Delta)} + \frac{1}{2})$ obtained unconditionally for the heralded atomic state $\hat{\rho}_W^{(A)}$. In principle, the imbalances in the interferometer can rotate the projectors into non-orthonormal sets (ref.[38], chapter 7). However, the measured losses and the beam-splitter ratios are sufficiently balanced such that any changes in $F^{(A)}$ due to modified projectors are well within the uncertainties of the data, as evidenced by the close-to-unity projection fidelity $F^{(\pi)} = 99.9^{+0.1}_{-0.2}\%$ (section 9.13.3). In the experiment, $\tilde{p}_1$ and F_1 are determined from the inferences of the spin-wave statistics (via y_c), and of the coherences (via Δ), respectively.

9.13.3 Numerical optimizations of the uncertainty bounds and their errors

In the presence of technical imperfections in the verification interferometer arising from imbalances in transmission losses $\{\eta, \eta'\}$ and beamsplitting ratios $\{\alpha, \alpha'\}$ of Fig. 9.5, the ideal projectors $\hat{\Pi}_i^{(c)} = |W_i\rangle_v\langle W_i|$ evolve into modified sets $\hat{\pi}_i^{(c)} = |W_i'\rangle_v\langle W_i'|$, which project the input $\hat{\rho}_r$ onto imbalanced W-states $|W_i'\rangle_v$, with chapters 7–8 providing further details. Generally, these projectors $\hat{\pi}_i^{(c)}$ are non-orthonormal due to the differential losses, but still span the single-excitation subspace $\hat{\rho}_1$ of $\hat{\rho}_r$. Importantly, the reductions of projection fidelities $F_i^{(\pi)} = {}_v\langle W_i|\hat{\pi}_i^{(c)}|W_i\rangle_v \leq 1$ of $\hat{\pi}_i^{(c)}$ can only decrease the *efficacy* of the verification protocol for detecting larger sets of states that belong to the state space of genuine W-states. Therefore, the observation of Δ below the bounds $\Delta_b^{(M-1)}$ using the modified projectors is still a sufficient condition for genuine M-partite entanglement (ref.[38], chapter 7). In the experiment, the losses and beamsplitter ratios for the interferometer are matched within 5%, as shown in Table 9.1.

To quantify the accuracies of our projectors $\pi_i^{(c)}$ to those of an ideal Δ-measurement, we numerically simulate the projection fidelities $F_i^{(\pi)}$ of the modified $\hat{\pi}_i^{(c)}$, as implemented by the measurement apparatus in Fig. 9.4b, to the ideal $\hat{\Pi}_i^{(c)}$. For this, we assume normal distributions for the parameters in Table 9.1 due to their systematic uncertainties, and build histograms of $F_i^{(\pi)}$ in Fig. 9.6, which give the probability densities $p_d(F_i^{(\pi)})$ for $F_i^{(\pi)}$ such that $\int_0^1 p_d dF_i^{(\pi)} = 1$. Due to the quadratic structure of the projection fidelities, $F_i^{(\pi)}$ is insensitive to small variations in the parameters of Table 9.1 when the verification interferometer is close to balanced (i.e., $\alpha_{12} \simeq \alpha_{34} \simeq \alpha_{14}' \simeq \alpha_{23}' \simeq 1/2$, $\eta_1 \simeq \eta_2 \simeq \eta_3 \simeq \eta_4$, and $\eta_1' \simeq \eta_2' \simeq \eta_3' \simeq \eta_4'$). Thus, we find a mean value $F^{(\pi)}$ of the four projection fidelities with $F^{(\pi)} = \frac{1}{4}(F_a^{(\pi)} + F_b^{(\pi)} + F_c^{(\pi)} + F_d^{(\pi)}) = 99.9^{+0.1}_{-0.2}\ \%$ by fitting the resulting probability densities $p_d^{(i)}$ to asymmetric Gaussian distributions $G(F_i^{(\pi)})$. The close-to-unity $\{F_i^{(\pi)}\}$ justify our analysis of the entanglement fidelities $\{F^{(A)}, F^{(\gamma)}\}$ for the atomic and photonic states.

In addition, we extend this model to numerically minimize the uncertainty bounds $\{\Delta_b^{(3)}, \Delta_b^{(2)}, \Delta_b^{(1)}\}$ over the full range of y_c for tripartite, bipartite entangled states, and for fully separable states, respectively (refs.[35,38], chapters 7–8). The calibration errors in the parameters of Table 9.1 give rise to the bands in the uncertainty bounds of Figs. 9.2 and 9.3, which depict the ± 1 s.d. uncertainties of the respective boundaries. In Fig. 9.7, we show the probability distributions of the bounds $\{\Delta_b^{(3)}, \Delta_b^{(2)}, \Delta_b^{(1)}\}$ for the minimal entanglement parameters $\{\Delta^{\min}, y_c^{\min}\}$ achieved in section 9.5.

Table 9.1: **Experimental imperfections in verification interferometer.** Measured beamsplitter values $\{\alpha, \alpha'\}$ and transmission efficiencies $\{\eta, \eta'\}$ for the verification interferometer in Fig. 9.5 are shown. The systematic uncertainties $(\delta\kappa)$ of $\{\kappa\}$ are fractionally $(\delta\kappa/\kappa) = 0.05$ for $\kappa \in \{\alpha, \alpha', \eta, \eta'\}$. Note that $\alpha_{12} \simeq \alpha_{34} \simeq \alpha_{14}' \simeq \alpha_{23}' \simeq 1/2$, $\eta_1 \simeq \eta_2 \simeq \eta_3 \simeq \eta_4$, and $\eta_1' \simeq \eta_2' \simeq \eta_3' \simeq \eta_4'$.

α_{12}	α_{34}	α_{23}'	α_{14}'	η_1	η_2	η_3	η_4	η_1'	η_4'	η_2'	η_3'
0.51	0.49	0.50	0.48	0.52	0.54	0.52	0.50	0.95	0.96	0.91	0.93

9.13.4 Data and error analysis

The calibration errors in Table 9.1 and the finite quantum efficiencies η_d for the non-number resolving (threshold) detectors D_i may cause the actual entanglement parameters $\{\Delta, y_c\}$ of the physical states $\{\hat{\rho}_W^{(A)}, \hat{\rho}_W^{(\gamma)}\}$, that result from the ideal POVM values of $\{\hat{\Pi}_i^{(c)}, \hat{\Pi}_i^{(s)}\}$, to be inferred incorrectly from our measurements. We describe here how $\{\Delta, y_c\}$ can be conservatively estimated from the photoelectron statistics of the detectors D_i.

First, we confine our analysis to the reduced subspace $\hat{\rho}_r = p_0\hat{\rho}_0 + p_1\hat{\rho}_1 + p_{\geq 2}\hat{\rho}_{\geq 2}$ of the physical density matrices $\{\hat{\rho}_W^{(A)}, \hat{\rho}_W^{(\gamma)}\}$ up to one excitation per mode and ensemble. Importantly, this truncation process can be simulated by local filters on the individual modes of $\{\hat{\rho}_W^{(A)}, \hat{\rho}_W^{(\gamma)}\}$ and leads to a *model-independent*

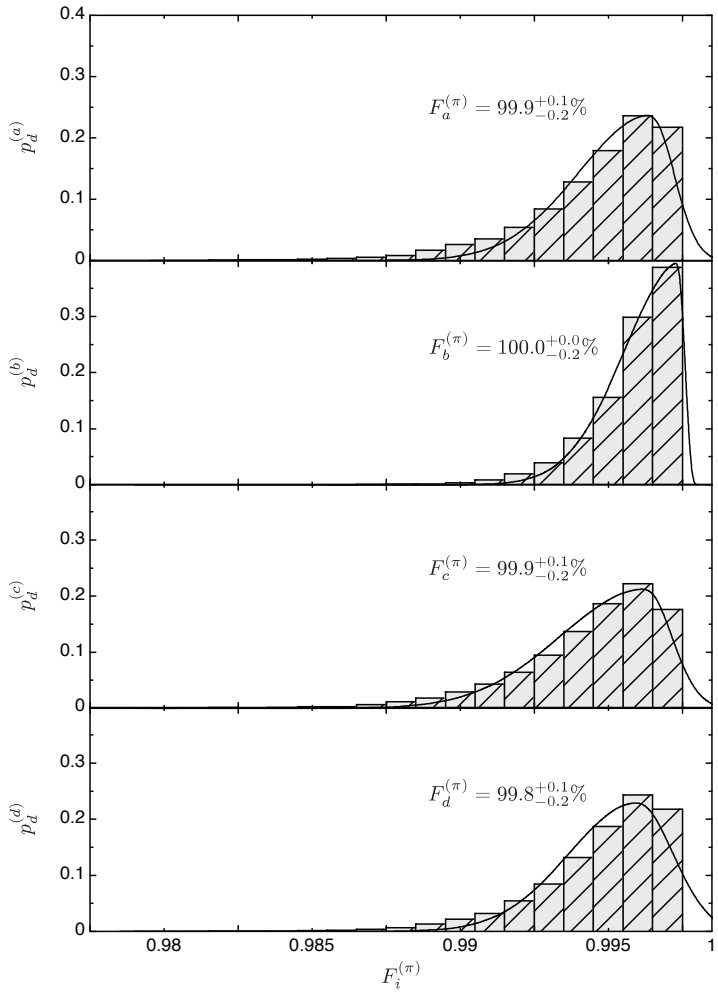

Figure 9.6: **Projection fidelities for quantum uncertainty relations.** We show histograms for the projection fidelities $F_i^{(\pi)}$ of the modified operator $\hat{\pi}_i^{(c)}$ to the ideal $\hat{\Pi}_i^{(c)}$ associated with detector D_i for $i \in \{a, b, c, d\}$. The mean value of the projection fidelities of $99.9^{+0.1}_{-0.2}$ % is deduced by fitting the respective probability densities $p_d^{(i)}$ with asymmetric Gaussian distributions $G(F_i^{(\pi)})$ (see the main text).

inference of the lower-bound entanglement of the full physical state $\{\hat{\rho}_W^{(A)}, \hat{\rho}_W^{(\gamma)}\}$ (ref.[27,34,110], chapter 3). The truncations of $\{\hat{\rho}_W^{(A)}, \hat{\rho}_W^{(\gamma)}\}$ into $\hat{\rho}_r$ also justify the use of single-photon avalanche photodetectors for the (local) y_c-measurement, since threshold detectors with finite efficiencies can be simulated by local filters[110]. We extract the photon statistics for the diagonal elements $\{p_0, p_1, p_{\geq 2}\}$ of $\hat{\rho}_r$ by a Bernoulli inversion[170] of the photoelectron statistics at D_i to the photon statistics q_{ijkl} at the faces of the ensembles (ref.[35], chapter 8). The spin-wave statistics can then be deduced by back-propagating the field statistics at the face of the ensembles to the spin-wave statistics $\{\tilde{p}_0, \tilde{p}_1, \tilde{p}_{\geq 2}\}$ for the reduced subspace of the ensembles, assuming linear mapping from matter to light (refs.[30,34], chapters 3 and 6).

For the sum uncertainty Δ, we additionally employ a numerical algorithm that estimates the upper bound of Δ for the one-excitation subspace $\hat{\rho}_1$. By defining the success probability $q_i^{(s)}$ for a single-photoelectric detection event $\overline{p}_i$ to arise from $\hat{\rho}_1$, the single-photoelectron probability $\overline{p}_i$ is given by (ref.[38], chapter 7),

$$\overline{p}_i = q_i^{(s)} p_i^{(s)} + (1 - q_i^{(s)}) p_i^{(f)}. \tag{9.5}$$

Here, $p_i^{(s)} = \mathrm{Tr}(\hat{\pi}_i^{(c)} \hat{\rho}_1)$ is the conditional probability for one photon at D_i originating from $\hat{\rho}_1$, normalized with $\sum_i p_i^{(s)} = 1$. On the other hand, $p_i^{(f)}$ is the normalized probability for a false single-photon event based on a spurious detection of a single photoelectron. Such an event can occur with a failure probability $1 - q_i^{(s)}$ if multiple photons are transmitted and registered at the same detector as a single photoelectron, or if the higher-order terms $\hat{\rho}_{\geq 2}$ at the faces of the ensembles are transformed into a single photon before the detectors by the lossy propagations (Table 9.1). Eq. 8.12 of chapter 8 (refs.[35,38]) provides the explicit expression for $q_i^{(s)}$. We do not subtract spurious backgrounds from atomic fluorescence, scattering noise, and detector dark counts.

Then, our goal is to unambiguously determine an upper bound of $\Delta = 1 - \sum_i (p_i^{(s)})^2$ for all possible realizations of $p_i^{(f)}$. We constrain this optimization problem with a set of data for the measured single-photoelectron probabilities $\overline{p}_i$ (Δ-measurement) and the photon statistics y_c (thereby, $\{p_0, p_1, p_{\geq 2}\}$ of $\hat{\rho}_r$), as well as the transmission efficiencies in Table 9.1 and the detection efficiencies for D_i. With these parameters, we assign the success probability $q_i^{(s)}$ of projecting the purported state $\hat{\rho}_r$ onto $\hat{\pi}_i^{(c)}$. Instead of algebraically upper bounding Δ (ref.[38], see chapters 7–8), which can yield an unphysically large result $\Delta > 0.75$, we perform a Monte-Carlo analysis to numerically determine a set of $p_i^{(s)}$ that maximizes Δ within the physical limit $\sum_i p_i^{(f)} = 1$ over the distributions of $q_i^{(s)}$. Here, the errors of $q_i^{(s)}$ occur from the systematic uncertainties of $\{\eta, \eta'\}$ and of the detection efficiencies, as well as of the statistical uncertainties of y_c of $\hat{\rho}_r$.

This procedure was employed for all the data sets of Figs. 9.2 and 9.3 (as well as of Figs. 9.8–9.10) to obtain conservative estimates of the entanglement parameters $\{\Delta, y_c\}$. The numerical errors for the Monte-Carlo simulations of all the data and the boundaries are well within $< 0.1\%$ of their overall uncertainties. In Fig. 9.7, we display a histogram for the minimal entanglement parameters $\{\Delta^{\min}, y_c^{\min}\} = \{0.07^{+0.01}_{-0.02}, 0.038 \pm 0.006\}$ (section 9.5). We find that $\Delta^{\min}$ (black bars) is suppressed below $\Delta_b^{(3)} =$

$0.261^{+0.010}_{-0.015}$ (red bars) by 10 s.d. We emphasize that we do not subtract any noise in the detection statistics nor do we post-select our data in the analysis, and thereby characterize the quantum state $\{\hat{\rho}_W^{(A)}, \hat{\rho}_W^{(\gamma)}\}$ that is physically available to the user.

9.14 Details on the theoretical model for the quantum interface

We describe theoretical models for the generation, storage, and transfer of the multipartite atomic state $\hat{\rho}_W^{(A)} = \mathrm{Tr}_h(\hat{\Pi}_h \hat{U}_{\text{write}}^\dagger \hat{\rho}_g^{(A)} \hat{U}_{\text{write}})$ to the photonic state of $\hat{\rho}_W^{(\gamma)} = \mathrm{Tr}_A(\hat{U}_{\text{read}}^\dagger \hat{\rho}_W^{(A)} \hat{U}_{\text{read}})$.

9.14.1 Entanglement generation

As we discussed in chapter 2, we begin our model with an interaction Hamiltonian (ref.[4])

$$\hat{H}_{\text{write}}^{(\epsilon)}/\hbar = \frac{g_0 \Omega_{\text{write}}^{(\epsilon)}}{\delta} (\hat{a}_{\gamma_1} \hat{S}_\epsilon + \hat{a}_{\gamma_1}^\dagger \hat{S}_\epsilon^\dagger) \tag{9.6}$$

for the parametric writing process of ensemble ϵ with excitation parameter $\xi = \tanh(g_0 \int \Omega_{\text{write}}^{(\epsilon)}(t) dt/\delta)$. Here, $\Omega_{\text{write}}^{(\epsilon)}$ (δ) is the Rabi frequency (detuning) of the writing laser, and $\hat{a}_{\gamma_1}$ ($\hat{S}_\epsilon$) is the annihilation operator for the fields γ_1 (collective excitations in ensemble ϵ). The writing process transforms the initial atomic state $|\overline{g}_\epsilon\rangle$ into individual products of two-mode squeezed states between the fields γ_1 and ensembles ϵ via $\hat{U}_{\text{write}} = \prod_\epsilon \exp(i \Delta t_w \hat{H}_{\text{write}}^{(\epsilon)}/\hbar)$, with the writing phases $\{\phi_1^{(w)}, \phi_2^{(w)}, \phi_3^{(w)}\}$ included in $\Omega_{\text{write}}^{(\epsilon)}$.

Upon the transformation of the fields γ_1 by our heralding interferometer, we find that the output mode operator for γ_1 is given by (up to an overall normalization) $\hat{a}_h \mapsto \hat{a}_{a_1} + e^{i\phi_1^{(h)}} \hat{a}_{b_1} + e^{i\phi_2^{(h)}} (\hat{a}_{c_1} + e^{i\phi_3^{(h)}} \hat{a}_{d_1})$, where $\hat{a}_{i_1}$ is the mode operator for the field $i_1 \in \gamma_1$. Here, we omit the vacuum terms because we make

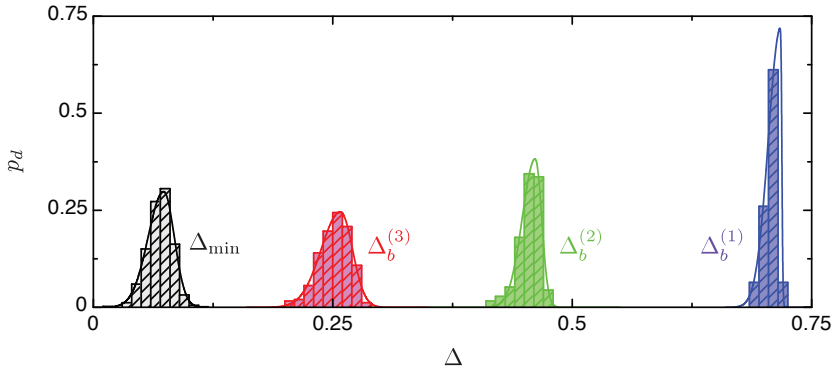

Figure 9.7: **Numerical optimizations for the minimal entanglement parameters and the uncertainty bounds.** Histograms of a Monte-Carlo analysis for minimizing 1-mode bound $\Delta_b^{(1)}$ (purple bars), 2-mode bound $\Delta_b^{(2)}$ (green bars), and 3-mode bound $\Delta_b^{(3)}$ (red bars) are shown for the smallest measured values of the entanglement parameters $\{\Delta^{\min}, y_c^{\min}\}$ (black bars) in section 9.5. The vertical axis is the probability density p_d corresponding to the respective value of Δ. The lines are fits to Gaussian distributions $p_d(\Delta) = G(\Delta)$ with asymmetric widths for ± 1 s.d.

use of normally ordered expectation values. Additionally, the heralding measurement $\hat{\Pi}_h$ with the threshold detector D_h is modeled with η_h, describing the overall efficiency for detecting γ_1 (including losses in the heralding channels, quantum efficiency of D_h and mode-matching efficiency to the collective state[74]), where

$$\hat{\Pi}_h = 1 - \sum_{n=0}^{\infty} \frac{:(-\eta_h \hat{a}_h^\dagger \hat{a}_h)^n:}{n!}. \tag{9.7}$$

Therefore, by calculating $\hat{\rho}_W^{(A)} = \mathrm{Tr}_h(\hat{\Pi}_h \hat{U}_{\text{write}}^\dagger \hat{\rho}_g^{(A)} \hat{U}_{\text{write}})$ for $\hat{\rho}_g^{(A)} = |\overline{g}_\epsilon\rangle\langle\overline{g}_\epsilon|$ and $\eta_h \ll 1$, we obtain the analytic expression of the atomic state $\hat{\rho}_W^{(A)}$ in Eq. 9.3 in the ideal case without additional noise (see section 9.14.4 for our noise model). The atomic entangled state $\hat{\rho}_W^{(A)}$ is thereby obtained non-destructively from a quantum measurement $\hat{\Pi}_h$ on the heralding systems γ_1, whereby the higher-order contamination $\hat{\rho}_{\geq 2}^{(A)}$ scales with ξ instead of ξ^2. The creation of $\hat{\rho}_W^{(A)}$ is then heralded by the photoelectric detection $\hat{\Pi}_h$ of the fields γ_1 with probability $p_h = \mathrm{Tr}(\hat{\Pi}_h \hat{U}_{\text{write}}^\dagger \hat{\rho}_g^{(A)} \hat{U}_{\text{write}})$.

9.14.2 Entanglement transfer

The transfer of the stored quadripartite entanglement to the photonic entanglement is described by a linear mapping process $\hat{U}_{\text{read}}$ (ref.[86], chapter 2), which transfers the delocalized collective state $|\overline{s}_\epsilon\rangle$ of the ensembles ϵ to the individual fields γ_2 with retrieval efficiency η_{read}. The reading process then generates a photonic state $\hat{\rho}_W^{(\gamma)} = \mathrm{Tr}_A(\hat{U}_{\text{read}}^\dagger \hat{\rho}_W^{(A)} \hat{U}_{\text{read}})$ via a 'beamsplitter' rotation $\hat{U}_{\text{read}}$ of $\hat{\rho}_W^{(A)}$ into $\hat{\rho}_W^{(\gamma)}$ with a ratio given by η_{read} (and reading phases $\{\phi_1^{(r)}, \phi_2^{(r)}, \phi_3^{(r)}\}$), after which the atomic states are traced over.

9.14.3 Entanglement verification

Finally, we model the photoelectric detection statistics of the photonic state $\hat{\rho}_W^{(\gamma)}$ at $D_{a,b,c,d}$. The detection probabilities for the output channels $\gamma_2' = \{a_2', b_2', c_2', d_2'\}$ of the entanglement verification setups in Figs. 9.4b and 9.5 can be modeled with projectors

$$\hat{\Pi}_0^{(\gamma_2')} = \sum_{n=0}^{\infty} \frac{:(-\eta_{\gamma_2'} \hat{a}_{\gamma_2'}^\dagger \hat{a}_{\gamma_2'})^n:}{n!} \tag{9.8}$$

for null events, and

$$\hat{\Pi}_1^{(\gamma_2')} = 1 - \hat{\Pi}_0^{(\gamma_2')} \tag{9.9}$$

for events that register one or more photons. Here, $\eta_{\gamma_2'}$ is the overall efficiency for detecting a photon in field γ_2' at $D_{a,b,c,d}$.

The photoelectric detection probabilities $\overline{p}_{ijkl}^{(c,s)}$ for counting i,j,k,l photoelectrons at $D_{a,b,c,d}$ can be calculated from the projectors $\hat{\Pi}_{ijkl}^{(c,s)} = \hat{\Pi}_i^{(a_2')} \hat{\Pi}_j^{(b_2')} \hat{\Pi}_k^{(c_2')} \hat{\Pi}_l^{(d_2')}$, via $\overline{p}_{ijkl}^{(c,s)} = \mathrm{Tr}(\hat{\Pi}_{ijkl}^{(c,s)} \hat{\rho}_W^{(\gamma)})$, for the respective configurations $\{c,s\}$ of Δ and y_c setups in Fig. 9.4b. Finally, the mode operator $\hat{a}_{\gamma_2'}$ for the output channel γ_2' is given by $(\hat{a}_{a_2'}, \hat{a}_{b_2'}, \hat{a}_{c_2'}, \hat{a}_{d_2'})^T = \hat{U}^{(c,s)} \cdot (\hat{a}_{a_2}, \hat{a}_{b_2}, \hat{a}_{c_2}, \hat{a}_{d_2})^T$. Here, the transfer matrix $\hat{U}^{(c,s)}$ is (i) a

unity matrix $\hat{U}^{(s)} = \mathbf{I}$ for the y_c-measurement, and (ii)

$$\hat{U}^{(c)} = \frac{1}{2}\begin{pmatrix} 1 & e^{i\beta_1} & e^{i\beta_2} & e^{i(\beta_2+\beta_3)} \\ 1 & -e^{i\beta_1} & -e^{i\beta_2} & e^{i(\beta_2+\beta_3)} \\ 1 & -e^{i\beta_1} & e^{i\beta_2} & -e^{i(\beta_2+\beta_3)} \\ 1 & e^{i\beta_1} & -e^{i\beta_2} & -e^{i(\beta_2+\beta_3)} \end{pmatrix} \tag{9.10}$$

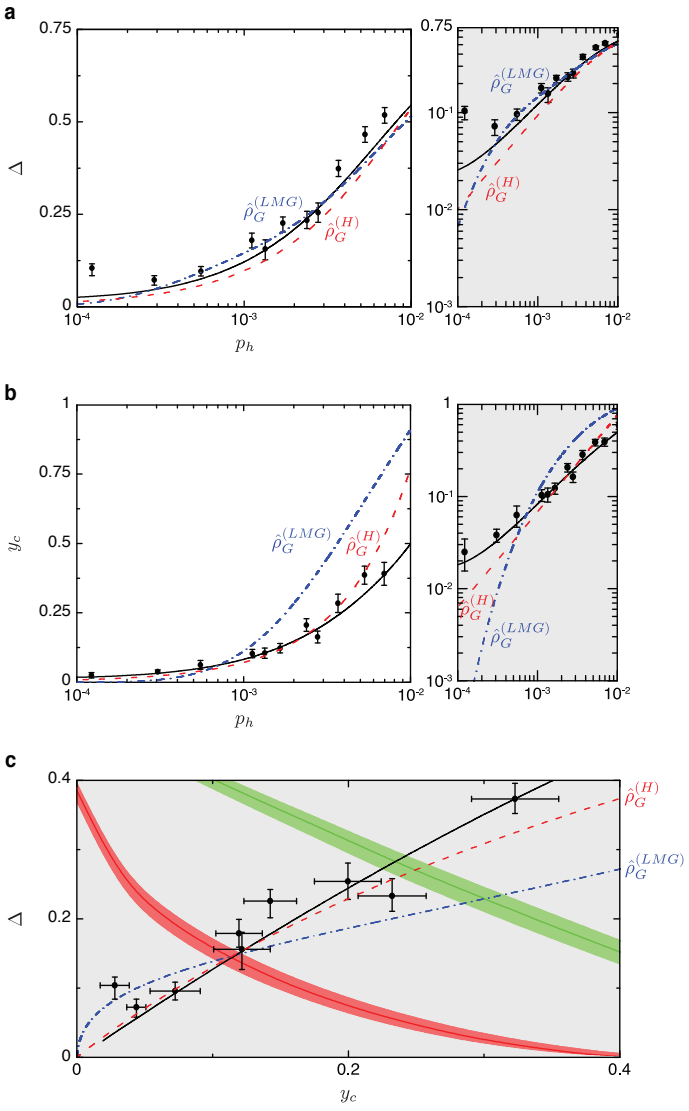

Figure 9.8: **Statistical evolutions of the individual entanglement parameters.** The data points and black line depict the statistical dependences of **a,** Δ and **b,** y_c to the heralding probability $p_h(\xi)$ for Fig. 9.2b. **c,** We also display the expanded view of the entanglement parameters $\{\Delta, y_c\}$ depicting the statistical transitions of multipartite atomic entanglement (inset of Fig. 9.2b). The thermal behaviors $\{\Delta^{(T)}, y_c^{(T)}\}$ of the thermal equilibrium states $\hat{\rho}_G^{(\mathrm{H})}$ and $\hat{\rho}_G^{(\mathrm{LMG})}$ of the Heisenberg-like and the Lipkin-Meshkov-Glick models are shown as red dashed and blue dash-dotted lines, respectively. Here, the horizontal axis is the heralding probability $p_h(\xi)$, with thermal excitation given by $\xi = e^{-\beta_T J}$ for the spin models.

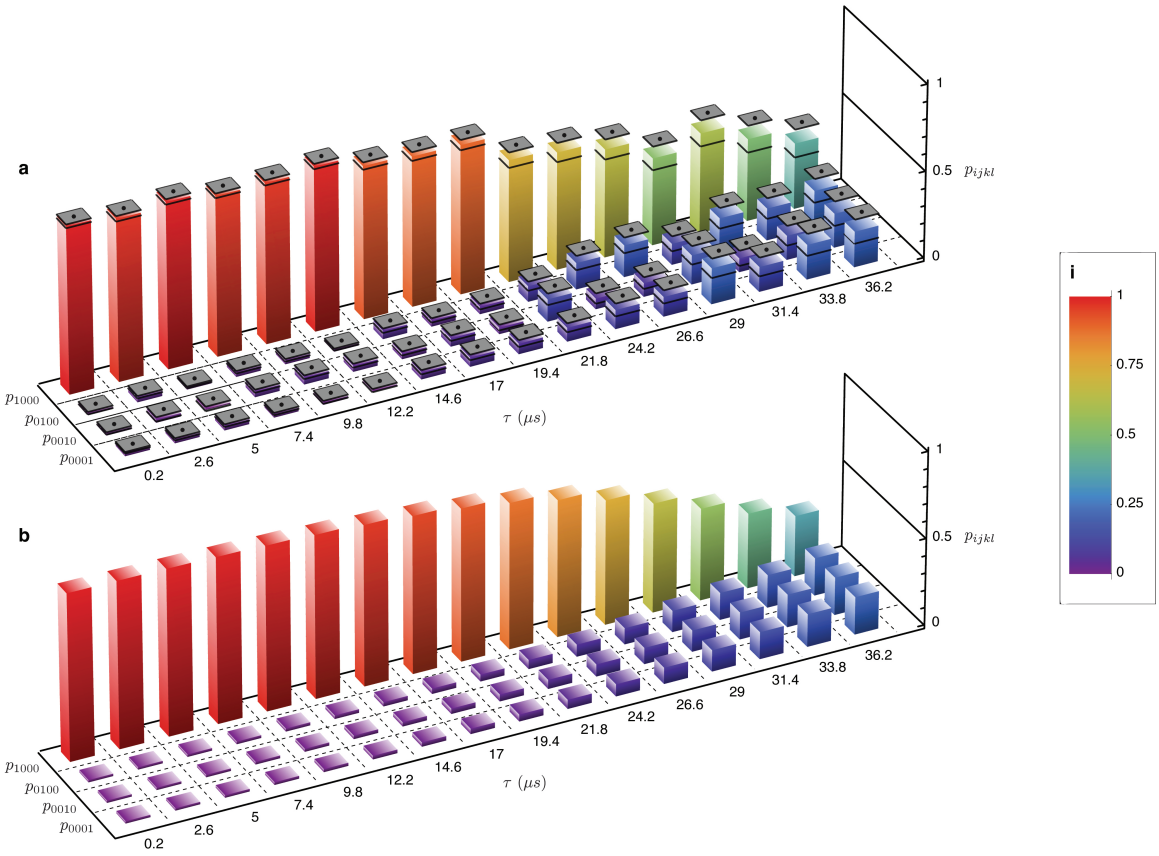

Figure 9.9: **Temporal decay of coherences stored in four atomic ensembles. a,** Evolution of the photon probabilities $\{p_{1000}, p_{0100}, p_{0010}, p_{0001}\}$ for occupying the output modes of the verification interferometer (Δ-measurement) versus storage time τ. For readability, the heights of the bars are shown in accord to the color convention of the inset **i**. Error bars, shown as grey squares, reflect the statistical uncertainties for each point. **b,** Photon probabilities $\{p_{1000}, p_{0100}, p_{0010}, p_{0001}\}$ from our theoretical model, which assumes a memory time determined from the temperature of the cold atomic samples and the net momentum transfer to the atomic spin-waves (chapter 2).

for the Δ-measurement (Fig. 9.5), where we assume balanced loss in writing Eq. 9.10, but not for our general analysis.

9.14.4 Incorporating noise into the model

To include the effects of atomic fluorescence and laser scattering noise emanating from the writing and reading processes, as well as of the background contamination including dark counts in the detectors, we mix dephased coherent states $\hat{\rho}_{r_B,q} = \int ||r_B|e^{i\phi_q}\rangle_q\langle|r_B|e^{i\phi_q}|d\phi_q$ and $\hat{\rho}_{r_I,q} = \int ||r_I|e^{i\phi_q}\rangle_q\langle|r_I|e^{i\phi_q}|d\phi_q$ into quantum channels $q \in \{\gamma_1, \gamma_2\}$ of the initial state, and find that

$$\hat{\rho}_g^{(A)} = \prod_{\epsilon} |\overline{g}_\epsilon\rangle\langle\overline{g}_\epsilon| \prod_{\gamma_1} (\hat{\rho}_{r_B,\gamma_1} \otimes \hat{\rho}_{r_I,\gamma_1}) \prod_{\gamma_2} (\hat{\rho}_{r_B,\gamma_2} \otimes \hat{\rho}_{r_I,\gamma_2}), \tag{9.11}$$

with quantum fields $\gamma_1 = \{a_1, b_1, c_1, d_1\}, \gamma_2 = \{a_2, b_2, c_2, d_2\}$. Here, $\{r_B, r_I\}$ are the respective probability amplitudes for the background and intensity-dependent noises (atomic fluorescence and scattering noise). In the experiment, we directly measure the noises $|r_{B,\gamma_1}|^2$, $|r_{B,\gamma_2}|^2$, and $|r_{I,\gamma_2}|^2$. We also infer the heralding and retrieval efficiencies $\{\eta_h, \eta_{\text{read}}\}$, as well as the scattering noise $|r_{I,\gamma_1}|^2 \propto |\Omega^{(\epsilon)}_{\text{write}}|^2$ for the writing laser by independently measuring the individual quantum correlation functions g_{γ_1,γ_2} for the fields $\{\gamma_1, \gamma_2\}$, following the methods in refs.[30,34,74] and chapters 3, 6.

Finally, using the initial state of $\hat{\rho}^{(A)}_g$ in Eq. 9.11, we approximate the physical state of $\hat{\rho}^{(A)}_W = \text{Tr}_h(\hat{\Pi}_h \hat{U}^\dagger_{\text{write}} \hat{\rho}^{(A)}_g \hat{U}_{\text{write}})$. We then simulate $\hat{\rho}^{(\gamma)}_W = \text{Tr}_A(\hat{U}^\dagger_{\text{read}} \hat{\rho}^{(A)}_W \hat{U}_{\text{read}})$ as well as the various expectation values of $\langle \hat{\Pi}^{(c,s)}_{ijkl} \rangle$ associated with the photoelectron statistics $\overline{p}^{(c,s)}_{ijkl}$ of $\{\Delta, y_c\}$. Finally, we perform the numerical algorithm described in section 9.13.4 and obtain the theoretical expectations of $\{\Delta_{\text{th}}, (y_c)_{\text{th}}\}$ as functions of heralding probability p_h, shown in Fig. 9.8. The theoretical curves in Fig. 9.2 are given by the parametric dependences of the entanglement parameters $\{\Delta_{\text{th}}, (y_c)_{\text{th}}\}$ to the heralding probability p_h.

9.14.5 Temporal dynamics of atomic multipartite entanglement

As described in section 9.9, the decoherence mechanism for the atomic W-state $\hat{\rho}^{(A)}_W(\tau)$ is dictated primarily by the motional dephasings of spin-waves (ref.[82], chapter 2). Qualitatively, the dephasings of the ensembles $\epsilon = \{a, b, c, d\}$ arise from independent evolutions of the spatial phases $\phi^{(sw)}_j(\tau) = \delta\vec{k} \cdot \vec{r}_j(\tau) + \phi_i$ imprinted on the spin-waves $|\overline{s}_\epsilon(\tau)\rangle = \sum_j e^{i\phi^{(sw)}_j(\tau)} |g \cdots s_j \cdots g\rangle_\epsilon$ due to thermal motions, where $\delta\vec{k} = \vec{k}_w - \vec{k}_1$ and $\phi_i = \phi^{(w)}_i - \phi^{(h)}_i$. Specifically, by assuming a Boltzmann velocity distribution with a mean velocity v_t for each ensemble ϵ, we find analytically that the probability p_c for the coherent atomic component $\hat{\rho}^{(A)}_c$ of $\hat{\rho}^{(A)}_W(\tau)$ decays over time τ, following $p_c \propto |\langle \overline{s}_\epsilon(0) | \overline{s}_\epsilon(\tau) \rangle|^2 \simeq e^{-\tau^2/\tau^2_m} + \mathcal{O}(1/N_{A,\epsilon})$ (refs.[82,114], chapter 2).

We follow a procedure similar to section 9.14 to simulate the dynamics of the atomic W-state $\hat{\rho}^{(A)}_W(\tau)$. In particular, absent any noise (i.e., $\hat{\rho}^{(A)}_g = |\overline{g}_\epsilon\rangle\langle\overline{g}_\epsilon|$) and for $\eta_h \ll 1$, we obtain the atomic dynamics

$$\begin{aligned} \hat{\rho}^{(A)}_W(\tau) \quad &\simeq \quad (1 - 3\xi)(\cos^2\theta(\tau)\hat{\rho}^{(A)}_c + \sin^2\theta(\tau)\hat{\rho}^{(A)}_n) \\ &\quad +3\xi\hat{\rho}^{(A)}_{\geq 2} + \mathcal{O}(\xi^2), \end{aligned} \tag{9.12}$$

where the mixing angles are $\cos^2\theta(\tau) = e^{-\tau^2/\tau^2_m}$ and $\sin^2\theta(\tau) = 1 - e^{-\tau^2/\tau^2_m}$. Thus, the decoherence for the atomic W-state results from the incoherent mixing of the initial superradiant state $\hat{\rho}^{(A)}_c \simeq |W\rangle_A\langle W|$ at $\tau = 0$ to mixtures of subradiant states $\hat{\rho}^{(A)}_n$ at $\tau > 0$, which increase the vacuum component $\hat{\rho}_0$ for the photonic state $\hat{\rho}^{(\gamma)}_W$. In turn, the increase of the subradiant states $\hat{\rho}^{(A)}_n$ contributes to a reduction in the coherent component $\hat{\rho}^{(A)}_c$ of $\hat{\rho}^{(A)}_W(\tau)$, as well as to a build-up of uncorrelated atomic noise $\hat{\rho}^{(A)}_{\geq 2}$ relative to $\hat{\rho}^{(A)}_c$. The net effect is a simultaneous degradation of the entanglement parameters $\{\Delta, y_c\}$ with a time-scale $\tau_m = 1/(|\delta\vec{k}|v_t) \simeq 17\ \mu s$. For the actual simulations in Fig. 9.2, we perform the full calculations including

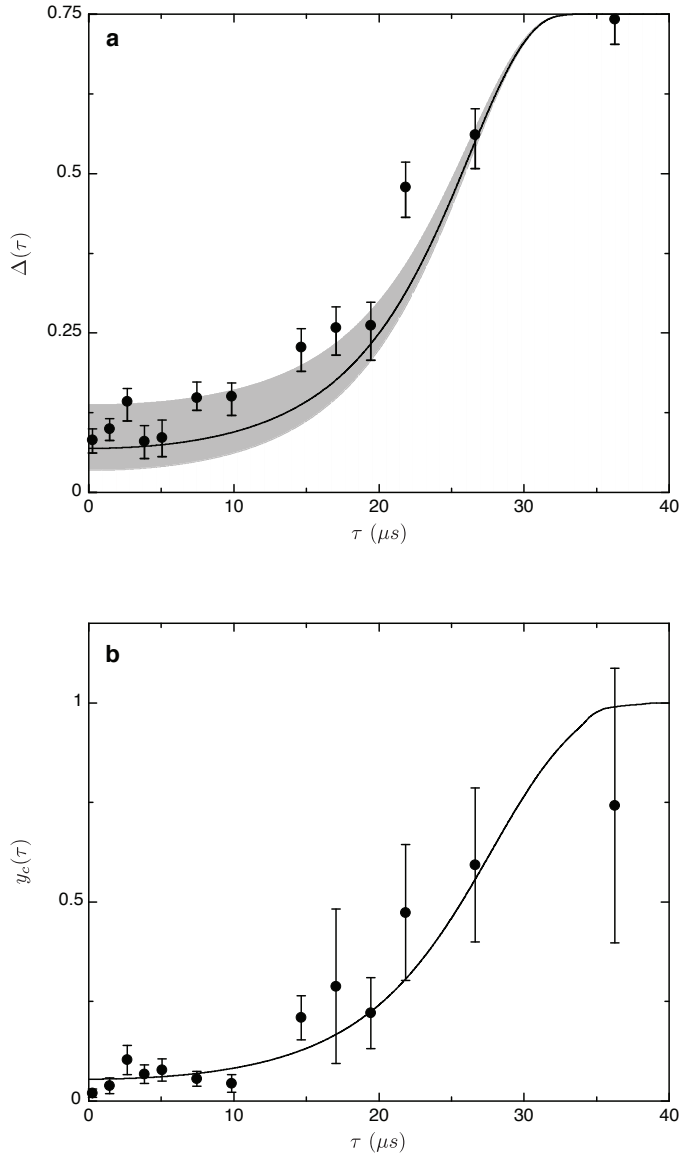

Figure 9.10: **Temporal evolutions of the individual entanglement parameters.** Due to the motional dephasings of the spin-waves, the experimentally measured entanglement parameters (black points), for **a,** $\Delta(\tau)$, and for **b,** $y_c(\tau)$, increase with a time-scale $\tau_m \simeq 17\mu s$. The theoretical simulation for the temporal behavior of $\{\Delta, y_c\}$ is displayed as a black solid line. The gray band around the theoretical curve $\delta(\tau)$ represents the $1/e$ uncertainty of the simulation due to the systematic error of the measured overlap $\overline{\lambda}$.

section 9.14 to incorporate the atomic fluorescence, laser scattering, and background noise.

Fig. 9.9 illustrates the temporal reduction in the overall coherence $\overline{d}$ of the full quadripartite state in our experiment (see section 9.6). Operationally, the loss of coherence is observed in terms of the decrease in imbalances among $\{p_{1000}, p_{0100}, p_{0010}, p_{0001}\}$ as a function of storage time τ, and hence to an increase in Δ. The behavior of the experimentally observed photon probabilities in Fig. 9.9a results from the progressive decay of the initial coherence for $\hat{\rho}_W^{(A)}(\tau_0)$ at $\tau_0 = 0.2\ \mu s$ for which $V_{\text{eff}}(\tau_0) = 4\overline{d} = 0.95 \pm 0.02$, evolving

then to $V_{\text{eff}}(\tau_f) = 0.10^{+0.25}_{-0.10}$ for the final state $\hat{\rho}_W^{(A)}(\tau_f)$ measured at $\tau_f = 36.2$ μs. The observed evolution is qualitatively in good agreement with our theoretical model of the photon probabilities shown in Fig. 9.9b. The spin-wave statistics are similarly modified by phase decoherence leading to an increase of y_c, from $y_c(\tau_0) = 0.03 \pm 0.01$ to $y_c(\tau_f) = 0.74 \pm 0.34$.

Finally, in Fig. 9.10, we show the dissipative dynamics of the atomic W-state (section 9.6), displayed independently for $\Delta(\tau)$ (Fig. 9.10a) and $y_c(\tau)$ (Fig. 9.10b). The complete 3-dimensional dynamics of the atomic W-states is displayed in Fig. 9.3. The temporal behaviors of $\{\Delta(\tau), y_c(\tau)\}$ in our experiment of the quadripartite atomic state (black points) are in qualitatively good agreement with the simulated dynamics for $\hat{\rho}_W^{(A)}(\tau)$ (black line). However, for Δ, we find that our data points consistently lie above the theoretical dynamics for $\hat{\rho}_W^{(A)}(\tau)$.

One possible explanation is that for the Δ-measurement, stringent interferometric stabilities and excellent overlaps $\overline{\lambda}$, close to unity, are required for all the 16 spatio-temporal modes $\{\vec{k}, s\}$, composed of the 8 quantum fields $\gamma_1 = \{a_1, b_1, c_1, d_1\}$ and $\gamma_2 = \{a_2, b_2, c_2, d_2\}$, as well as of the 8 classical writing and reading pulses, with s corresponding to the polarization state of each field. Ultimately, the wavepacket overlap for the entangled fields $\gamma_2 = \{a_2, b_2, c_2, d_2\}$ is limited by the differential optical depths of the cold samples $\{a, b, c, d\}$, which in turn yield differential group velocities during the slow light process of coherent transfer from $\hat{\rho}_W^{(A)}$ to $\hat{\rho}_W^{(\gamma)}$ by way of dynamic electromagnetically induced transparency (ref.[86], chapter 2).

We include this effect in the model via a field overlap $\overline{\lambda}$ (ref.[150]), where a fit corresponding to Fig. 9.8 gives $\overline{\lambda} = 0.98$ ($\overline{\lambda} = 0.95$ for Fig. 9.10a), with similar results obtained from the calculation of overlap for the measured temporal shapes of the wave-packets $\gamma_2 = \{a_2, b_2, c_2, d_2\}$. For the simulated dynamics of Fig. 9.3a (section 9.6), we use the field overlaps $\overline{\lambda}$ obtained independently from classical measurements of the interferometric visibility for both 'classical' (write, read) and 'quantum' interferometers (quantum fields γ_1, γ_2). Thus, the discrepancy in $\Delta(\tau)$ can be largely attributed to the systematic uncertainty in the inference of $\overline{\lambda} = 0.97 \pm 0.03$, with the uncertainty corresponding to the dynamics of $\Delta(\tau)$ shown as a gray band in Fig. 9.10a.

9.15 Entanglement thermalization

Here, we formulate the thermal equilibrium state $\hat{\rho}_G$ (refs.[39,297]) of a Heisenberg-like model $\hat{H}_{\rm H}$ and a Lipkin-Meshkov-Glick model $\hat{H}_{\rm LMG}$, as presented in Fig. 9.2b of section 9.5 (see also Fig. 9.8c). We compare the entanglement parameters $\{\Delta^{(T)}, y_c^{(T)}\}$ obtained from $\hat{H}_{\rm H}$ and $\hat{H}_{\rm LMG}$ to the observed statistical behavior of the quadripartite states of the ensembles.

9.15.1 Heisenberg-like model

We begin with a Heisenberg-like Hamiltonian $\hat{H}_{\rm H}$ of four ($N_s = 4$) spins $\{i, j\}$ of spin vectors $\vec{S}^{(i)} = \{\hat{S}_x^{(i)}, \hat{S}_y^{(i)}, \hat{S}_z^{(i)}\}$ with isotropic infinite-ranged ferromagnetic interaction ($J_{ij} = J > 0$ for all $\{i, j\}$), where

$$\hat{H}_{\rm H} = -\frac{J}{N_s}\sum_{\langle i,j\rangle}\vec{S}^{(i)}\cdot\vec{S}^{(j)} + h_z\sum_i \hat{S}_z^{(i)} + \hat{H}_p.$$

Here, $\hat{H}_{\rm H}$ includes a standard Heisenberg interaction $-\frac{J}{N_s}\sum_{\langle i,j\rangle}\vec{S}^{(i)}\cdot\vec{S}^{(j)} + h_z\sum_i \hat{S}_z^{(i)}$, as well as a spin-projection term $\hat{H}_p = 2h_z|S,-S\rangle\langle S,-S|$ which selects out the collective spin state $|S,-S\rangle$ with bias energy $2h_z$ and suppresses the thermal equilibrium population of $|S,-S\rangle$.

Since the Hamiltonian $\hat{H}_{\rm H}$ commutes with the collective spin operators $\{\vec{S}^2, \hat{S}_z\} \equiv \{(\sum_i \vec{S}^{(i)})^2, \sum_i \hat{S}_z^{(i)}\}$, $\hat{H}_{\rm H}$ is diagonal in the basis of collective spin states $|S, M\rangle$ for $0 \le S \le N_s/2$ and $-S \le M \le S$. The eigenenergies are

$$\mathcal{E}_{S,M} = \begin{cases} -\frac{J}{4}S(S+1) + h_z M + \frac{3J}{4}, & \text{if } |S,M\rangle \neq |2,-2\rangle \\ -\frac{3J}{4}, & \text{if } |S,M\rangle = |2,-2\rangle. \end{cases}$$

The degeneracy for $|S, M\rangle$ is given by $D_S = \frac{(2S+1)N_s!}{(N_s/2+S+1)!(N_s/2-S)!}$ (ref.[170]). Importantly, for any value of $h_z > 0$, the ground state is $|2,-1\rangle \equiv |W_1\rangle = \frac{1}{2}(|1000\rangle + |0100\rangle + |0010\rangle + |0001\rangle)$ with energy $\mathcal{E}_{2,-1} = -\frac{3J}{4} - h_z$. In the following sections, we will set the magnetic field to $h_z = J/2$.

9.15.2 Thermal equilibrium state

We solve for the Gibbs state, $\hat{\rho}_G^{(\rm H)} = \frac{1}{Z}e^{-\beta_T \hat{H}_{\rm H}}$, where $Z = {\rm Tr}(e^{-\beta_T \hat{H}_{\rm H}})$ is the partition function and beta parameter $\beta_T = 1/k_B T$ for thermal energy $k_B T$ at temperature T. Explicitly, we obtain $\hat{\rho}_G^{(\rm H)} = \frac{1}{Z}\sum_{S,M} D_S e^{-\beta_T \mathcal{E}_{S,M}}\hat{\rho}_{S,M}$. Here, the component $\hat{\rho}_{S,M}$ is a mixed state that contains all possible $|S, M\rangle$ for the degeneracy of D_S; e.g., $\hat{\rho}_{1,-1} = \frac{1}{3}(|W_2\rangle\langle W_2| + |W_3\rangle\langle W_3| + |W_4\rangle\langle W_4|)$ is a mixture of three non-symmetrized single-excitation W-states, $\{|W_2\rangle, |W_3\rangle, |W_4\rangle\}$.

By mapping the spin-states to number-states ($|\downarrow,\uparrow\rangle \mapsto |0,1\rangle$) [a], we obtain a Gibbs number-state $\hat{\rho}_G^{(n)}$ in the form of

$$\hat{\rho}_G^{(n)}(T) = p_0\hat{\rho}_0 + p_1\hat{\rho}_1 + p_{\ge 2}\hat{\rho}_{\ge 2}, \tag{9.13}$$

[a] Physically, the transfer of the spin-states to number-states can be accomplished by coherent mapping to photons.

as in the reduced density matrices $\hat{\rho}_r$ of $\{\hat{\rho}_W^{(A)}, \hat{\rho}_W^{(\gamma)}\}$. Our goal is to calculate the thermal (T) behavior of multipartite entanglement[39,297] for $\hat{\rho}_G^{(n)}$ via the entanglement parameters $\{\Delta^{(T)}, y_c^{(T)}\}$.

Because the vacuum component $\hat{\rho}_0$ and the higher-order terms $\hat{\rho}_{\geq 2}$, as well as the non-symmetric single-excitation states $\hat{\rho}_{1,-1}$ of $\hat{\rho}_1$ are more energetic than the ground state $|W_1\rangle$, the Gibbs state $\hat{\rho}_G^{(n)}(T=0)$ is the symmetric W-state $|W_1\rangle\langle W_1|$ at zero temperature. For low temperature ($\beta_T \gg 1$), we approximate $\hat{\rho}_G^{(n)}$ by

$$\hat{\rho}_G^{(n)}(T) \simeq Z_0\hat{\rho}_0 + Z_1\hat{\rho}_1 + (1 - Z_1 - Z_0)\hat{\rho}_{\geq 2}, \tag{9.14}$$

with $Z_0 = e^{\frac{3\beta_T J}{4}}$ and $Z_1 = Z_W + 3Z_X$. The single-excitation subspace $\hat{\rho}_1$ is

$$\hat{\rho}_1(T) \simeq \frac{1}{Z_1}(Z_W|W_1\rangle\langle W_1| + 3Z_X\hat{\rho}_{1,-1}), \tag{9.15}$$

with $Z_W = e^{\frac{\beta_T(4h_z+3J)}{4}}$, $Z_X = e^{\frac{\beta_T(4h_z-J)}{4}}$. Here, the thermal excitations from the ground state $|W_1\rangle\langle W_1|$ to one of $\hat{\rho}_{1,-1}$ occur with probability $\xi = Z_X/Z_W = e^{-\beta_T J}$.

9.15.3 Entanglement parameters

For the sum uncertainty $\Delta^{(T)}$, we only consider the single-excitation subspace $\hat{\rho}_1$ (Eq. 9.15). The probability to find $|W_1\rangle$ is $p_{1000} = \langle W_1|\hat{\rho}_1|W_1\rangle = \frac{1}{1+3e^{-\beta_T J}}$, whereas the probabilities to find the non-symmetric states are $p_{0100} = p_{0010} = p_{0001} = \frac{e^{-\beta_T J}}{1+3e^{-\beta_T J}}$. For $\beta_T \gg 1$, we deduce the sum uncertainty $\Delta^{(T)} \simeq 6e^{-\beta_T J} = 6\xi$. Similarly, we find the quantum statistics $y_c^{(T)} \simeq \frac{16}{3}e^{-\beta_T J} = \frac{16}{3}\xi$. Thus, the parametric relation

$$\Delta^{(T)} \simeq 6 \times \frac{3}{16}y_c^{(T)} = \frac{9}{8}y_c^{(T)} \tag{9.16}$$

replicates the statistical behavior of $\Delta_{\text{th}} \simeq \frac{9}{8}(y_c)_{\text{th}}$ for the ensembles (section 9.14) in the low-excitation regime (equivalent to $\beta_T \gg 1$).

By performing the full calculation of $\{\Delta^{(T)}, y_c^{(T)}\}$ for $\hat{\rho}_G^{(n)}$ without any approximations and by inserting the excitation probability $\xi = e^{-\beta_T J}$ into the expression of heralding probability $p_h(\xi)$ for $\hat{\rho}_W^{(A)}$ (section 9.14), we compare the theoretical expectations $\{\Delta^{(T)}, y_c^{(T)}\}$ of the thermal state $\hat{\rho}_G^{(\text{H})}$ to the experimental data, presented in Fig. 9.2b as a red dashed line (section 9.5; see also Fig. 9.8c). In Fig. 9.8, we plot the dependences of the individual parameters $\Delta^{(T)}$ and $y_c^{(T)}$ to p_h as red dashed lines. The panels on the right-hand side show the log-log scale plots of the figures for small values of ξ.

9.15.4 Lipkin-Meshkov-Glick model

We simulate the entanglement parameters $\{\Delta^{(T)}, y_c^{(T)}\}$ of a thermal equilibrium state $\hat{\rho}_G^{(\mathrm{LMG})}$ for an isotropic Lipkin-Meshkov-Glick (LMG) Hamiltonian $\hat{H}_{\mathrm{LMG}}$ (refs.[298–300]), where

$$\hat{H}_{\mathrm{LMG}} = -\frac{J}{4}\sum_{\langle i,j\rangle}(\hat{S}_x^{(i)}\hat{S}_x^{(j)} + \hat{S}_y^{(i)}\hat{S}_y^{(j)}) + h_z\sum_i \hat{S}_z^{(i)},$$

with infinite-range interactions $J > 0$. The energy states are the collective spin states $|S, M\rangle$ with the eigenenergy $\mathcal{E}_{S,M} = -\frac{J}{4}(S(S+1) - M^2) + \frac{J}{2} + h_z M$. By setting $h_z = J/2$, the ground state can be made $|W_1\rangle$. Proceeding with the methods in sections 9.15.2–9.15.3, we calculate $\{\Delta^{(T)}, y_c^{(T)}\}$ for the Gibbs state $\hat{\rho}_G^{(\mathrm{LMG})}$ of $\hat{H}_{\mathrm{LMG}}$, as depicted in the blue dash-dotted lines of Fig. 9.8 and Fig. 9.2b.